Geophysical Journal International

Geophys. J. Int. (2020) **222,** 132–152
Advance Access publication 2020 March 28
GJI Marine geosciences and applied geophysics

doi: 10.1093/gji/ggaa152

Magmatic and tectonic segmentation of the intermediate-spreading Costa Rica Rift—a fine balance between magma supply rate, faulting and hydrothermal circulation

A.H. Robinson,[1] L. Zhang,[2] R.W. Hobbs,[1] C. Peirce[1] and V.C.H. Tong[2]

[1]*Department of Earth Sciences, Durham University, Durham, UK. E-mail: a.h.robinson@durham.ac.uk*
[2]*Department of Earth Sciences, University College London, London, UK*

Accepted 2020 March 20. Received 2020 March 5; in original form 2019 May 23

SUMMARY

3-D tomographic modelling of wide-angle seismic data, recorded at the intermediate-spreading Costa Rica Rift, has revealed a *P*-wave seismic velocity anomaly low located beneath a small overlapping spreading centre that forms a non-transform discontinuity at the ridge axis. This low velocity zone displays a maximum velocity anomaly relative to the 'background' ridge axis crustal structure of ∼0.5 km s^{-1}, has lateral dimensions of ∼10 × 5 km, and extends to depths ≥2.5 km below the seabed, placing it within layer 2 of the oceanic crust. We interpret these observations as representing increased fracturing under enhanced tectonic stress associated with the opening of the overlapping spreading centre, that results in higher upper crustal bulk porosity and permeability. Evidence for ongoing magmatic accretion at the Costa Rica Rift ridge axis takes the form of an axial magma lens beneath the western ridge segment, and observations of hydrothermal plume activity and microearthquakes support the presence of an active fluid circulation system. We propose that fracture pathways associated with the low velocity zone may provide the system through which hydrothermal fluids circulate. These fluids cause rapid cooling of the adjacent ridge axis and any magma accumulations which may be present. The Costa Rica Rift exists at a tipping point between episodic phases of magmatic and tectonically enhanced spreading. The characteristics inherited from each spreading mode have been preserved in the crustal morphology off-axis for the past 7 Myr. Using potential field data, we contextualize our seismic observations of the axial ridge structure at the whole segment scale, and find that the proposed balance between magmatic and tectonically dominated spreading processes observed off-axis may also be apparent along-axis, and that the current larger-scale magma supply system at the Costa Rica Rift may be relatively weak. Based on all available geophysical observations, we suggest a model for the inter-relationships between magmatism, faulting and fluid circulation at the Costa Rica Rift across a range of scales, which may also be influenced by large lithosphere scale structural and/or thermal heterogeneity.

Key words: Composition and structure of the oceanic crust; Hydrothermal systems; Controlled source seismology; Mid-ocean ridge processes.

1 INTRODUCTION

The ∼65 000 km ocean spreading ridge system encircles the globe, with the oceanic crust formed there facilitating ∼31 TW of heat flow from the inner Earth to hydrosphere (Davies & Davies 2010). Around a third of this heat flux is via hydrothermal circulation of fluid within the crust, the global flow of which has been estimated to be up to 0.35 Sv (Elderfield & Schultz 1996). In turn, about 0.12 Sv of this circulation occurs within young crust <1 Myr in age (Stein & Stein 1994), which facilitates chemical exchange between the solid Earth and hydrosphere and results in both transfer of minerals and alteration of crustal composition (Alt & Teagle 2000). Thus, the characteristics of mid-ocean ridge spreading processes result in a significant contribution to the long-term global flux of heat and fluids, and the formation of mineral deposits.

The structure of the crust formed at mid-ocean ridges is related to spreading rate, reflecting not only the thermal regime but also the volume and continuity of magma supply (Lin & Phipps Morgan 1992; Phipps Morgan & Chen 1993; Small & Abbott 1998; Liu & Buck 2018; Wilson *et al.* 2019). At intermediate spreading ridges, periodic fluctuations in magma supply also influence ridge axis morphology (e.g. Phipps Morgan & Chen 1993; Canales *et al.* 2005;

White *et al.* 2008), and control the dominant style of spreading at any time. As a result, crustal formation at intermediate spreading rates is thought to occur in a 'finely balanced' state between the two end-members of magmatic accretion and tectonic spreading, where changes of <3–5 mm yr^{-1} in the spreading rate may tip the balance between the two end members (Wilson *et al.* 2019).

In this study, we apply a range of geophysical techniques to characterize the formation and resultant structure of the crust at the intermediate-spreading Costa Rica Rift, to improve understanding of the interactions between magmatic and tectonic processes for this spreading rate classification. In particular, we aim to understand better how the balance between the predominance of magmatic versus tectonic spreading processes may control factors such as the ridge morphology and segmentation, and the potential existence of, and interaction between, both axial magma and hydrothermal circulation systems.

1.1 Spreading rate context

Long-term oceanic crustal thickness is generally uniform at all but the slowest (<15 mm yr^{-1}) full-spreading rates (FSR; e.g. White *et al.* 1992; Bown & White 1994). However, over shorter spatial and temporal scales, slower spreading ridges (<40 mm yr^{-1} FSR) have a greater range in crustal thickness (3–8 km) than faster ridges (>60 mm yr^{-1} FSR, 5–7 km thick; e.g. Chen 1992). Magmatically formed crust has a layered seismic velocity–depth structure (Houtz & Ewing 1976) that divides it into an upper basaltic layer (layer 2), and a lower gabbroic layer (layer 3). Layer 2 is further subdivided into an uppermost layer comprising extrusive, high porosity pillow basalts that is termed layer 2A at the ridge axis, which overlies layer 2B, which comprises sheeted dykes (Herron 1982; Christeson *et al.* 1992; Harding *et al.* 1993). The boundary between these layers is marked by a high vertical velocity gradient (1–2 s^{-1}; Grevemeyer *et al.* 2018a). For example, layer 2A thickness has been measured at 0.49–0.54 km close to the Blanco Transform, below which the transition to layer 2B occurs over 0.23–0.28 km (Christeson et al. 2010, 2012).

As the crust ages, seismic velocity increases due to cooling, hydrothermal alteration (Houtz & Ewing 1976; Christensen 1979; Carlson 1998), and the infilling of bulk porosity (Christensen 1978; Vera *et al.* 1990; Christeson *et al.* 2007). Typically, for crust younger than ∼0.5 Ma, layer 2A has a velocity of between 3.0 and 3.2 km s^{-1} (Christeson *et al.* 2012), while the top of layer 2B is more variable within the range ∼4.3–4.9 km s^{-1} (Newman *et al.* 2011; Christeson *et al.* 2012), with values increasing to 4.0–4.5 and ∼5.1–5.4 km s^{-1} respectively, by ∼5 Ma post-formation (Wilson *et al.* 2019).

Ultraslow and slow spreading ridges (<50 mm yr^{-1} FSR—e.g. the Southwest Indian Ridge, Mid-Cayman Spreading Centre and Mid-Atlantic Ridge, MAR) are characterized by an axial valley-type topography, with terraces formed by inward-facing, axis-parallel, normal faults and large-scale detachment surfaces. The latter exhume the lower crust and uppermost mantle at the seabed as oceanic core complexes (OCCs) and facilitate fluid ingress and serpentinization (e.g. Cann *et al.* 1997; Ranero & Reston 1999; Canales *et al.* 2004; Reston & Ranero 2011; Grevemeyer *et al.* 2018b; Peirce *et al.* 2019). This mode of spreading is highly variable in both space and time, as demonstrated by the prevalence of asymmetric spreading, alternation between which ridge flanks represent the footwall and hanging wall of the detachment surface, and the diversity of geological features exposed at and located below the seabed (e.g. Cannat 1993; Ranero & Reston 1999; Peirce *et al.* 2005; Cannat *et al.* 2006; Peirce & Sinha 2008; Reston 2018). Faster spreading ridges (>70 mm yr^{-1} FSR—e.g. the East Pacific Rise, EPR) have a shallower seabed topography and an axial rise (e.g. Detrick *et al.* 1993; Scheirer & Macdonald 1993). At this ridge type, basaltic lava flows and dykes of layer 2 are accreted symmetrically about the ridge axis, and comprise the relatively smooth topped upper oceanic basement (Sinton & Detrick 1992).

Intermediate spreading ridges (50–70 mm yr^{-1} FSR) such as the Juan de Fuca Ridge (JdFR, e.g. Hooft & Detrick 1995; Canales *et al.* 2005), the Galapagos Spreading Ridge (GSR, e.g. Detrick *et al.* 2002; Sinton *et al.* 2003; Blacic *et al.* 2004), the South East Indian Rise (SEIR, e.g. Cochran *et al.* 1997; Ma & Cochran 1997; Baran *et al.* 2005), and the Valu Fa Ridge in the Lau back-arc basin (VFR, Collier & Sinha 1992; Turner *et al.* 1999; Day *et al.* 2001) display morphologies that vary between the axial rise end-member of faster spreading ridges (JdFR, VFR) and the rift valleys typical of slower spreading ridges (SEIR) as well as exhibiting significant along-ridge variability (GSR).

1.2 Ridge axis characteristics

At faster spreading ridges (hereafter EPR-type), effectively steady-state magmatic accretion is inferred from seismic studies (e.g. Detrick 1987; Kent *et al.* 1990, 2000; Hooft *et al.* 1997; Singh *et al.* 1998; Marjanovic *et al.* 2018). High amplitude reflection events are interpreted as narrow, sill-like accumulations of predominantly molten rock that are commonly referred to as axial magma or melt lenses (AMLs). Basaltic magma erupts from an AML to form layer 2 (Sinton & Detrick 1992), but how the lower crust forms remains a topic of debate (Kelemen *et al.* 1997; Maclennan *et al.* 2005; Wanless & Shaw 2012).

AMLs typically have a thickness of <50–100 m and a width of <2 km (e.g. Detrick *et al.* 1987; Kent *et al.* 1990; Sinton & Detrick 1992; Canales *et al.* 2005; Carbotte *et al.* 2013). Although volumetrically small, their existence is a complex interplay between heat gain, principally by injection of new magma from below, and heat loss, by eruption and hydrothermal circulation from above (Fontaine *et al.* 2011; Lowell *et al.* 2013). Similar magma bodies have been identified at several EPR-type intermediate spreading ridges, including: the Endeavour, Northern Symmetric and Cleft Segments of the JdFR (Canales *et al.* 2005, 2009; Carbotte *et al.* 2006; van Ark *et al.* 2007); between 94°15′W and 91°00′W along the western GSR (Detrick *et al.* 2002; Blacic *et al.* 2004); the P1, P2 and P3 segments of the SEIR (Baran *et al.* 2005) and the VFR (Collier & Sinha 1992; Turner *et al.* 1999; Day *et al.* 2001). However, at intermediate ridges displaying characteristics of slower spreading systems, such as west of 95°30′W at the western GSR and the S1 segment of the SEIR, no magma bodies have been detected (Blacic *et al.* 2004; Baran *et al.* 2005). Where observed, AMLs tend to be located towards the middle of spreading segments, and increase in depth or disappear in the vicinity of offsets in ridge trend (Detrick 1987; Kent et al 2000, 2002; Canales *et al.* 2005; Carbotte *et al.* 2013). The existence of an AML may, therefore, be influenced by both along ridge structural variability and the rate of magma supply.

AMLs are only rarely observed at slower spreading ridges (hereafter MAR-type), such as the Reykjanes Ridge in the North Atlantic (e.g. Sinha *et al.* 1997, 1998; MacGregor *et al.* 1998; Navin *et al.* 1998). This does not mean that these systems are amagmatic, but instead that the magma supply is believed to be limited and episodic, with a short-lived injection prior to crystallization. Overall, the inter-relationships between axial morphology, evidence for active

magma supply and the thickness of seismic layer 2A (Buck *et al.* 1997) suggest that, together, these features are co-controlled by the distinct modes of crustal formation (Phipps Morgan & Chen 1993).

The mid-ocean ridge system is also, along its length, segmented by various scales of discontinuity (Macdonald *et al.* 1991). Macdonald *et al.* (1988) proposed a hierarchical model of ridge segmentation based on magma supply, with segment length decreasing from the largest first-order segments, separated from each other by large-offset transform faults, though a series of different crustal tectonic manifestations including non-transform offsets and overlapping spreading centres, to the shortest, fourth-order segments, that are characterized by small deviations in axial linearity (deval) or variation in geochemical composition.

An overlapping spreading centre (OSC) is a small-scale ridge axis discontinuity where two adjacent ridge segments are laterally offset by 1–10 km, and the ridge tips overlap each other by a similar distance (Macdonald & Fox 1983). Under the magma supply model of ridge segmentation (Macdonald *et al.* 1988), these features occur at the ends of adjacent magma supplied regions and are typically magma poor, and so undergo enhanced tectonic stretching that results in crustal thinning. Between the ridge tips, the bathymetry is typically deeper than the surrounding region by up to several hundred metres, and the tectonic fabric shows no predominant ridge-parallel or ridge-perpendicular (transform) alignment.

OSCs are inherently unstable and, thus, tend to evolve over time, with one of the limbs prevailing while the other is abandoned (Macdonald & Fox 1983). OSC evolution modelling (Wilson 1990; Macdonald *et al.* 1991; Baud & Reuschle 1997) predicts that the ridge tips initially deflect away from each other and then, later, curve sharply back towards one another, finally resulting in a characteristic ratio of overlap to offset of ~3:1 (Macdonald *et al.* 1984; Sempéré & Macdonald 1986). Eventually, the ridge segments may rejoin in a process known as self-decapitation (Macdonald *et al.* 1987). When the overlap between adjacent ridge segments is large, a relic trace may be left in the off-axis crust (e.g. Macdonald *et al.* 1984; Canales *et al.* 1997), akin to the large-scale pseudofaults associated with propagating rifts (e.g. Hey 1977).

Observations of axial magma lenses made in the vicinity of OSCs show a diversity of morphologies and interactions. At the EPR, for example, AMLs have been observed to deepen as they approach the 9°03′N and 11°45′N OSCs, relative to their mid-segment locations (Detrick 1987; Hooft *et al.* 1997). At 9°03′N (Kent *et al.* 2000; Tong *et al.* 2002) and 9°37′N–9°40′N (Han *et al.* 2014), the AMLs have an overlapping structure, mirroring that of the ridge tips on the seabed, suggesting that magma lenses can extend to segment ends. At the 9°17′N deval (Kent *et al.* 1993) and 5°30′S offset (Lonsdale 1983) at the EPR, and the ~22°S OSC at the intermediate-spreading VFR (Turner *et al.* 1999; Day *et al.* 2001), amongst others, magma lenses are observed to be continuous across such discontinuities.

2 COSTA RICA RIFT

2.1 Geological setting

The Costa Rica Rift (CRR) is the easternmost ridge segment of the Cocos-Nazca spreading centre, located in the Panama Basin in the Eastern Pacific (Fig. 1a). It extends for ~180 km and is bounded by the Ecuador Fracture Zone in the west, and the Panama Fracture

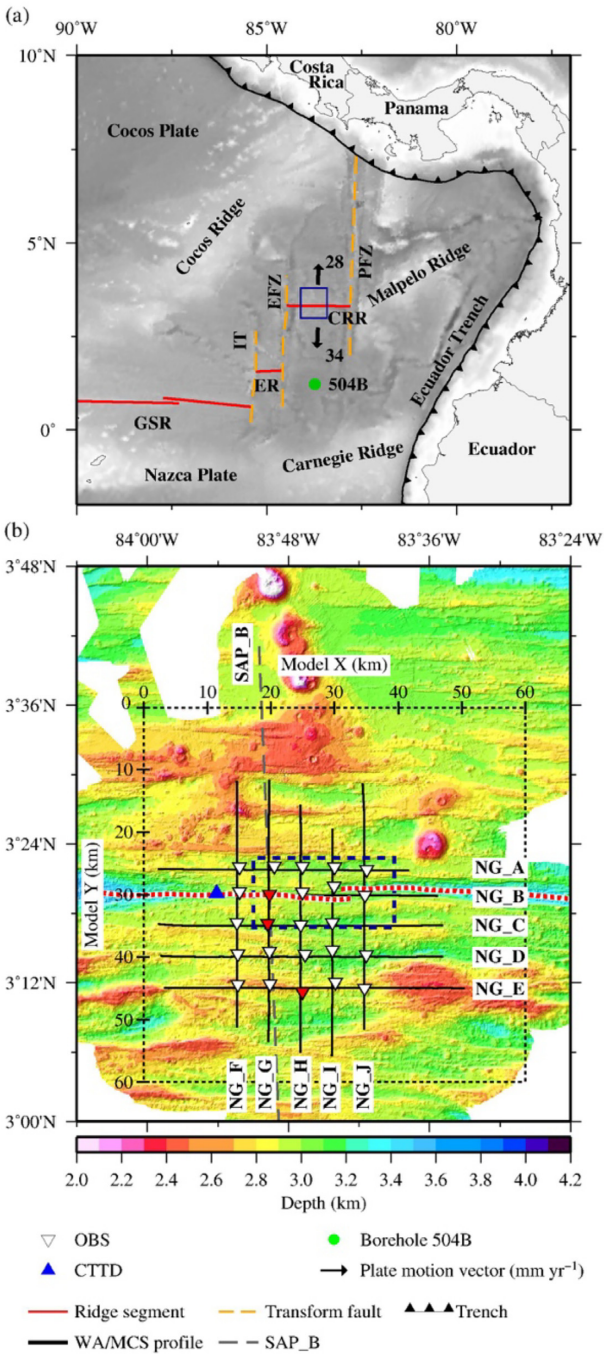

Figure 1. North Grid study area and regional bathymetry. (a) Principal regional tectonic features of the Panama Basin, plotted over GEBCO (2008) bathymetry. Blue box indicates area shown in (b). Plate motions are from NRR-MORVEL56 (Argus *et al.* 2011). CRR, Costa Rica Rift; ER, Ecuador Rift; GSR, Galapagos Spreading Ridge; PFZ, Panama Fracture Zone; EFZ, Ecuador Fracture Zone; IT, Inca Transform Fault. (b) Ship-acquired swath bathymetry of the CRR ridge axis. Layout of the North Grid seismic acquisition with profile names annotated. Dashed black box shows the extent of the 3-D model, with axes labelled in model co-ordinates. Dashed red line shows location of the ridge axis centre line. Red filled triangles indicate OBS with record sections shown in Fig. 4. Dashed blue box indicates region shown in Fig. 2(a).

Zone in the east. Spreading has been ongoing for 11 Myr (Londale & Klitgord 1978), and is presently occurring asymmetrically at an intermediate half-spreading rate of 30 mm yr^{-1} for the north flank (the Cocos Plate) and 36 mm yr^{-1} for the south (the Nazca Plate; Wilson & Hey 1995). Magnetic anomaly modelling demonstrates that significant variation in the spreading rate and degree of asymmetry has also occurred since spreading initiated (Wilson & Hey 1995; Wilson *et al.* 2019).

Over the past 6 Myr, several plate motion changes have occurred within the Panama Basin (Lonsdale & Klitgord 1978; Krijgsman *et al.* 1999; Morell 2015) which have influenced the stress regime and style of spreading. In particular, the collision of the Cocos and Carnegie aseismic ridges with Central and South America (Fig. 1a), which began between 1 and 2 Ma (Lonsdale & Klitgord 1978; Gutscher *et al.* 1999; Meschede & Barckhausen 2001), led to the suppression, impediment or slowing of northward and eastward plate motion, as recorded by the corresponding variation in spreading rate (Wilson & Hey 1995; Wilson *et al.* 2019).

Although classified as an intermediate spreading ridge, the CRR displays a MAR-type axial valley morphology, with a distinctive hourglass shape decreasing in width from ∼10 km at the segment ends to ∼3 km at its narrowest point. Divided into eastern and western limbs by an OSC-type non-transform ridge axis discontinuity located at 3°20′N, 83°44′W, the two segment halves overlap by ∼2.5 km, and are laterally offset by ∼1.5 km (Fig. 2a). Swath bathymetry data show that the shallowest portion of the ridge axis lies along the western limb at ∼2.9 km depth (Fig. 2b), in a region of recent volcanic activity (Buck *et al.* 1997; Haughton *et al.* 2018).

The OSC is similar in size to those located between 91°00′W and 95°30′W on the western GSR (Sinton *et al.* 2003), which forms the continuation of the Cocos-Nazca plate boundary to the west. However, it lies at the lower end of the size range for similar features observed along the slow-spreading MAR (Spencer *et al.* 1997) and Central Indian Ridge (Tyler *et al.* 2007), the intermediate-spreading JdFR (e.g. Canales *et al.* 2005; Weekly *et al.* 2014) and the fast-spreading EPR, (e.g. Lonsdale 1983, Macdonald & Fox 1983; Macdonald *et al.* 1984), at which much larger features have overlaps and offsets of ≥30 and ≥10 km, respectively.

In 1994, RV Maurice Ewing expedition EW9416 (Detrick 1994) imaged an AML ∼10 km to the west of the CRR OSC, between 83°48′W and 83°50′W, beneath the bathymetrically shallowest part of the ridge axis (Buck *et al.* 1997; Figs 2 and 3). This feature had a length of ∼2.4-km-along axis, and was located at 1.2–1.4 s two-way traveltime (TWTT) beneath the seabed reflection, equivalent to a depth of ∼3.0–3.5 km within the crust based on an average upper crustal velocity of 5 km s^{-1}. Conductivity, temperature and transmissometry versus depth (CTTD) observations made during an oceanographic survey of the entire Panama Basin (Fig. 1b; Morales Maqueda 2015; Lowell *et al.* 2020), sampled a hydrothermal plume above the ridge axis, close to the western termination of the AML. Using the AML dimensions and the measured heat output, modelling suggests that the magmatic system beneath the western limb of the CRR is relatively weak, and may be subject to either a low-level continuous replenishment or a more intermittent episodic recharge to maintain its stability (Lowell *et al.* 2020).

2.2 Aims of this study

We apply 3-D seismic tomographic modelling to determine the structure and characteristics of the upper oceanic crust at the CRR ridge axis, in the vicinity of the AML and OSC. We aim to determine not only how these features manifest in the crustal seismic velocity structure, but also whether and how they may inter-relate in terms of the processes underlying their formation and subsequent evolution over time. We also examine the possible relationship between tectonic processes and the location of observed hydrothermal venting at the ridge axis. Finally, we use potential field data to investigate the extent and controls on the larger, whole segment-scale magma distribution at the CRR, and how this relates to plate-scale tectonic processes. As part of this modelling, we investigate the role of inherited crustal and/or lithospheric fabric resulting from past plate reorganization, and how these impact on the spreading ridge system both in the Panama Basin, and when set in the wider plate tectonic context.

3 DATA ACQUISITION

The axial region of the CRR formed the focus of research expedition RRS James Cook JC114 (Hobbs & Peirce 2015), undertaken as part of the OSCAR (*Oceanographic and Seismic Characterization of heat dissipation and alteration by hydrothermal fluids at an Axial Ridge*) project. Throughout JC114, multibeam swath bathymetry data were acquired using a Kongsberg EM120 hull-mounted echosounder, calibrated using a sound velocity profile measured to the seabed within the study area. Gravity data were also acquired port-to-port using a LaCoste & Romberg Micro-G air-sea gravimeter, tied to absolute stations in Caldera (Costa Rica) and Panama City (Panama) at the start and end respectively (Hobbs & Peirce 2015). Magnetic data were acquired only during seismic surveying.

For 3-D tomographic imaging, an array of 25 ocean-bottom seismographs (OBSs) was deployed at the ridge axis, in a 5 × 5 km grid centred on 3°20′N, 83°44′W. The grid (henceforth the North Grid or NG; Fig. 1b) was connected via a flow-line profile (SAP_B; Wilson *et al.* 2019) to a matching grid (Gregory *et al.* 2017) located at ODP borehole 504B, ∼230 km to the south (Fig. 1a; Becker *et al.* 1989, and references therein) to provide geological ground-truth. Over the North Grid, colocated multichannel seismic (MCS) reflection and wide-angle (WA) refraction data were acquired along five E–W and five N–S profiles through the OBS array (Fig. 1b), including along an E–W profile along the ridge axis co-incident with the location of Profile 1268 of the EW9416 MCS survey, which originally detected the AML (Fig. 2a; Detrick *et al.* 1994). Both profiles are colocated to well within the width of the seismic Fresnel zone at AML depth, to accommodate any non-exact match in navigation, so should image the same subseabed region. Further details of the data acquisition are provided in Hobbs & Peirce (2015).

Shots were fired at 30 s intervals using a 1320 in^3 (21.63 l) six Bolt airgun array, towed at 8 m depth below sea surface. Each OBS recorded WA refracted arrivals at a sampling rate of 500 Hz, using a three-component geophone and hydrophone set. First arrival traveltimes were picked from the hydrophone data (Fig. 4) due to its higher signal-to-noise ratio, and because it contained the least scattered energy given the largely sediment-free seabed. Approximately 68 500 WA first arrivals were picked within a shot-receiver range of 2.3–36.5 km from each OBS. Traveltime picks were assigned an uncertainty, based on the shot-receiver offset (Table 1), to account for picking and instrument location errors. In the first instance, the majority of the picks, with the exception of those at the very shortest shot-receiver offsets, were assigned a uniform uncertainty of 45 ms.

In addition, between phases of active source seismic data acquisition, the NG OBS array also recorded microearthquakes over a

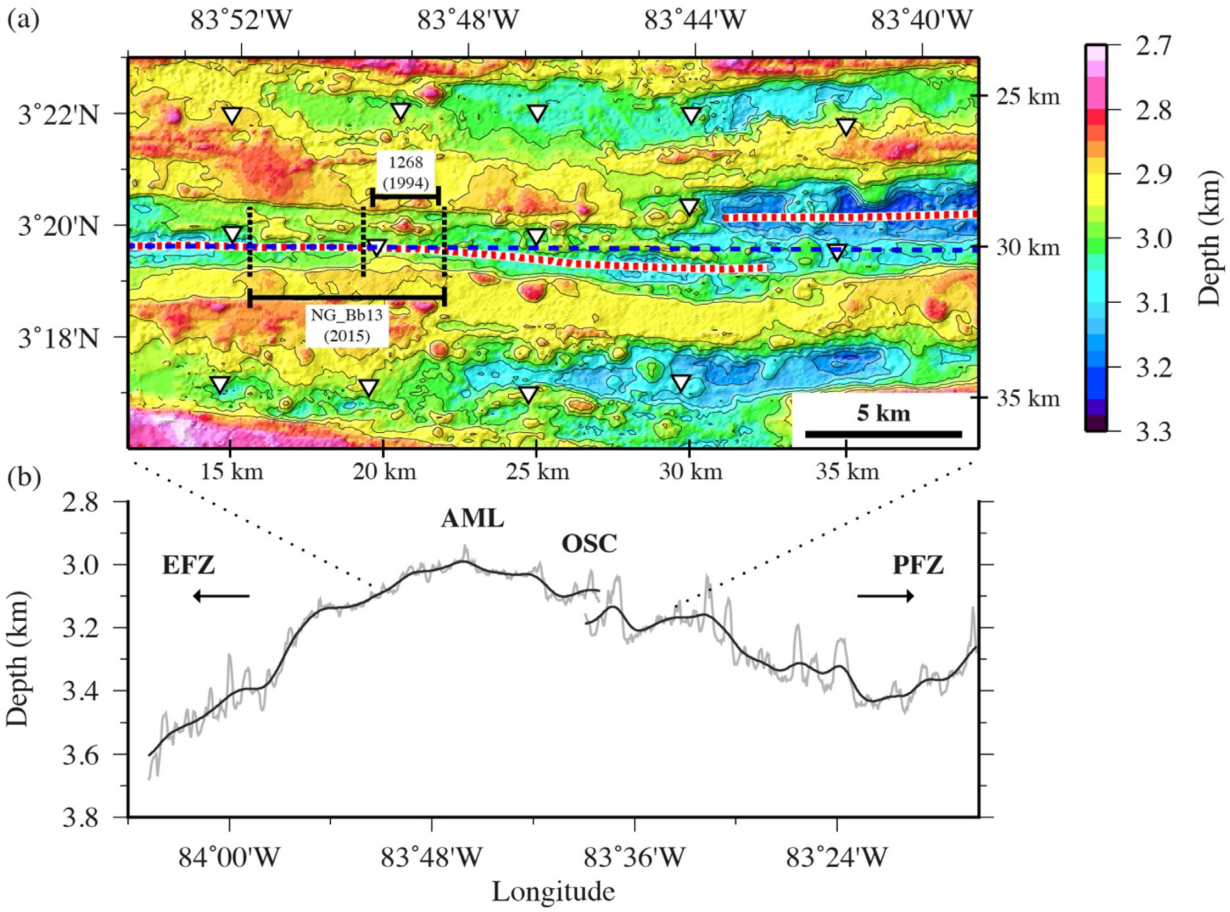

Figure 2. Swath bathymetry of the CRR showing ridge axis structure. (a) Ridge axis in the vicinity of the overlapping spreading segment. Red dashed line indicates the location of ridge axis centre line. Blue dashed line is the location of OSCAR MCS Profile NG_Bb13 (Lowell *et al.* 2020), co-incident with the location of EW9416 Profile 1268 (Buck *et al.* 1997). Dashed black lines show the longitudes of the ends of the observed AML from these two surveys. Inverted triangles show OBS locations (*cf.* Fig. 1b). (b) Bathymetry sampled along the ridge axis centre line (light grey), shown with a 3′ (∼5 km) Gaussian filter applied (dark grey). Dotted black lines show location relative to (a). Labelled arrows indicate the directions to and names of bounding fracture zones (*cf.* Fig. 1a). OSC and AML locations along the ridge axis are labelled.

21-day period (Lowell *et al.* 2020; Fig. 3). The locations of the 116 largest magnitude microearthquakes recorded during the survey period were estimated using the NonLinLoc software (Lomax *et al.* 2000), using a 1-D crustal velocity model derived from modelling of both OBS and MCS gather traveltime picks (this study and Wilson *et al.* 2019). Projection of event hypocentres onto a depth-converted image of EW9416 MCS Profile 1268 shows that the majority are distributed at, or above, the AML between 83°28.8′W and 83°31.2′W (Fig. 3b). The distribution of seismicity suggests two principal event populations. The events of the first cluster, occurring between Julian days 26 and 34, extend from the seabed to AML depth, and are located above or to the west of the AML. However, the events of the second cluster (days 35–47) generally lie deeper than 5 km below sea surface, and are located directly above the observed AML. No events are observed between the eastern observed limit of the AML and the OSC, however a small number of events may be associated with the latter.

4 TOMOGRAPHIC INVERSION

Traveltime picks were inverted in 3-D using FAST (First-Arrival Seismic Tomography; Zelt & Barton 1998). This approach treats all arrivals as diving rays and produces a smooth velocity model without discrete layer interfaces. The overall goal of an inversion is to minimize the traveltime residuals along ray paths to reach a χ^2 fit of 1, representing a fit to the specified error bounds. Consequently, if χ^2 becomes <1, the model is 'relaxed' by finding the largest value of the trade-off parameter (which controls the balance between minimizing the data misfit and generating a model with the minimum required structure) that results in a χ^2 of 1.

4.1 Initial model

The initial model (Fig. 5a) was parametrized on a 0.1 × 0.1 × 0.1 km uniform (cubic) forward grid within a 60 × 60 km model footprint. The origin (0,0 km in X,Y) of the model space was located at 3°35′N, 84°00′W (Fig. 1b), and offsets within the model were set to increase to the south and west. The seabed was constructed from the high-resolution swath bathymetry data and, because there is effectively no sediment cover within the NG, it could be regarded as the top of layer 2A within model discretization errors.

The lack of short-offset (<2.5 km) arrivals in the NG WA data set results in limited constraint on the uppermost crustal velocity. Consequently, the initial model was constructed using a 1-D velocity–depth profile extracted from Wilson *et al.*'s (2019) 2-D seismic model of Profile SAP_B (Fig. 5f), where it crosses the

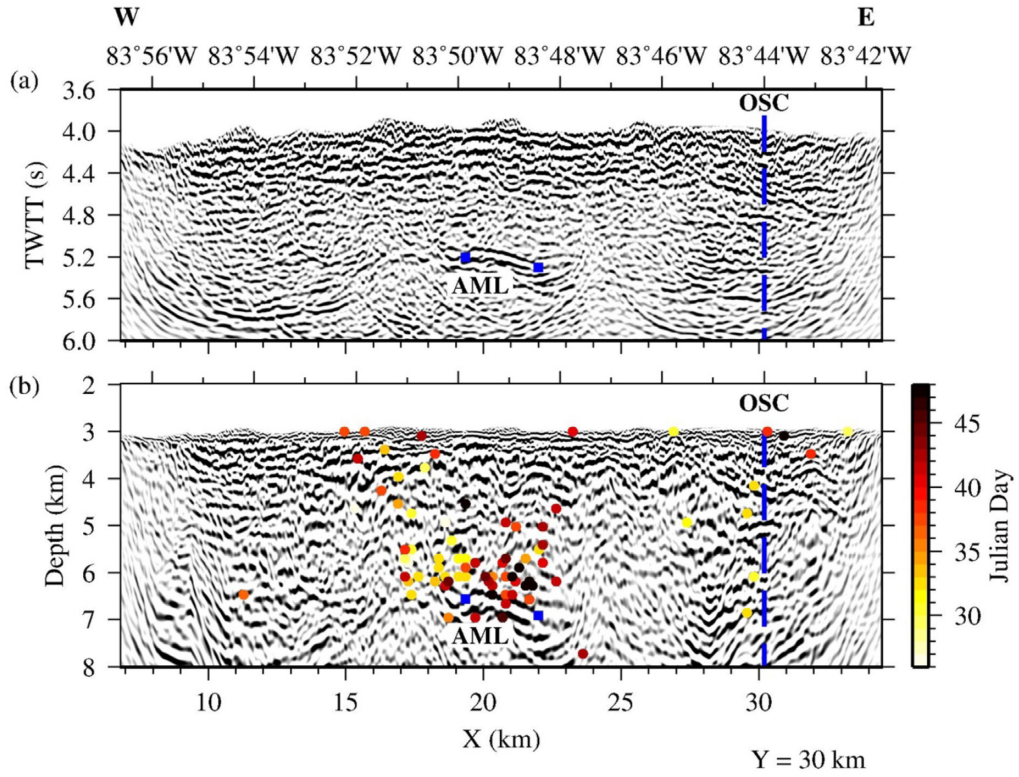

Figure 3. MCS image of the CRR AML from (a) EW9416 Profile 1268 (after Buck *et al.* 1997), adapted from Lowell *et al.* (2020). The blue squares indicate the along-ridge extent at ∼5.1–5.3 s TWTT. Location of the OSC is labelled. Upper annotations/tick-marks indicate actual location of the features shown, lower annotations/tick-marks show locations in NG model space. (b) Depth converted, migrated seismic image of Profile 1268. Dots show depths of relocated earthquake hypocentres located within ∼2 km of the plane of the profile, the majority of which plot directly above the AML. Events are coloured by Julian day in 2015, and show two temporal clusters between JD 26–34 (lighter/yellow) and 35–47 (darker/red).

ridge axis (Fig. 5b), added below the bathymetry (Fig. 5a). This model provides some independent constraint on the shallowest velocity structure in the subseabed region not well constrained by the NG data set, whilst not imposing a preconceived shallow structure throughout the NG footprint.

4.2 Inversion

To determine appropriate inversion parametrization, we tested a range of horizontal and vertical inverse cells sizes over which model smoothing and regularization were applied. This included combinations of lateral inverse cell sizes of 1.0 and 0.5 km (in both *X* and *Y*) and vertical (*Z*) cells of 0.2 and 0.5 km. Using the initial model described above, testing aimed to determine which configuration(s) resulted in:

(i) dense and consistent sampling of the model by rays;
(ii) good lateral resolution of potential features of interest, and;
(iii) consistent model structure with minimal artefacts.

In all cases, we applied a single-pass inversion process over a series of five iterations, each testing five values of the trade-off parameter. The results showed that, in all cases, the first iteration achieved a relatively good fit ($\chi^2 = 2.26$) and that the inversion converged to a χ^2 of ∼1 within 2–4 iterations, depending on the parametrization. From this point trade-off parameter 'relaxation' occurs, resulting in a final range of χ^2 values between 0.99 and 1.00 for the range of model parametrizations. The parameters consequently selected for the inversion are summarized in Table 2.

Vertical slices through the resulting best-fitting model (hereafter the *inversion model*) are shown in Figs 5(c)–(e) and horizontal slices in Fig. 6. The model has an overall $\chi^2 = 1.00$ and a root mean square misfit of 42 ms, and will be discussed in Section 5. Ray coverage throughout the *inversion model* was calculated by counting the ray hits for each 3-D inversion cell. By definition, smaller inverse cell sizes, in both lateral and vertical dimensions, will tend to decrease the number of observed ray hits. However, for all cell size combinations tested a consistent and dense ray coverage of >100 hits per cell was achieved beneath the OBS array over a model depth range of $Z = 3.7$–5.5 km, corresponding to a depth range of ∼0.7–2.5 km below seafloor (b.s.f.). The extent of ray coverage is used to mask all vertical and lateral slices to indicate where the *inversion model* is constrained.

4.3 Resolution testing

To determine whether velocity anomalies observed in the *inversion model* are well resolved, checkerboard testing was performed following the approach of Zelt & Barton (1998). A ±5 per cent velocity perturbation was added to the *inversion model* (Fig. 7a), taking the form of a columnar checkerboard pattern (Zelt 1998). This pattern was selected based on Zelt's (1998) assertion that, for 3-D tomographic inversion, horizontal resolution is primarily controlled by the ray coverage through the model, whilst vertical resolution is controlled by the background, or input model used for inversion, together with the vertical parametrization of the inversion approach. On this basis, since we use an independently derived and tested

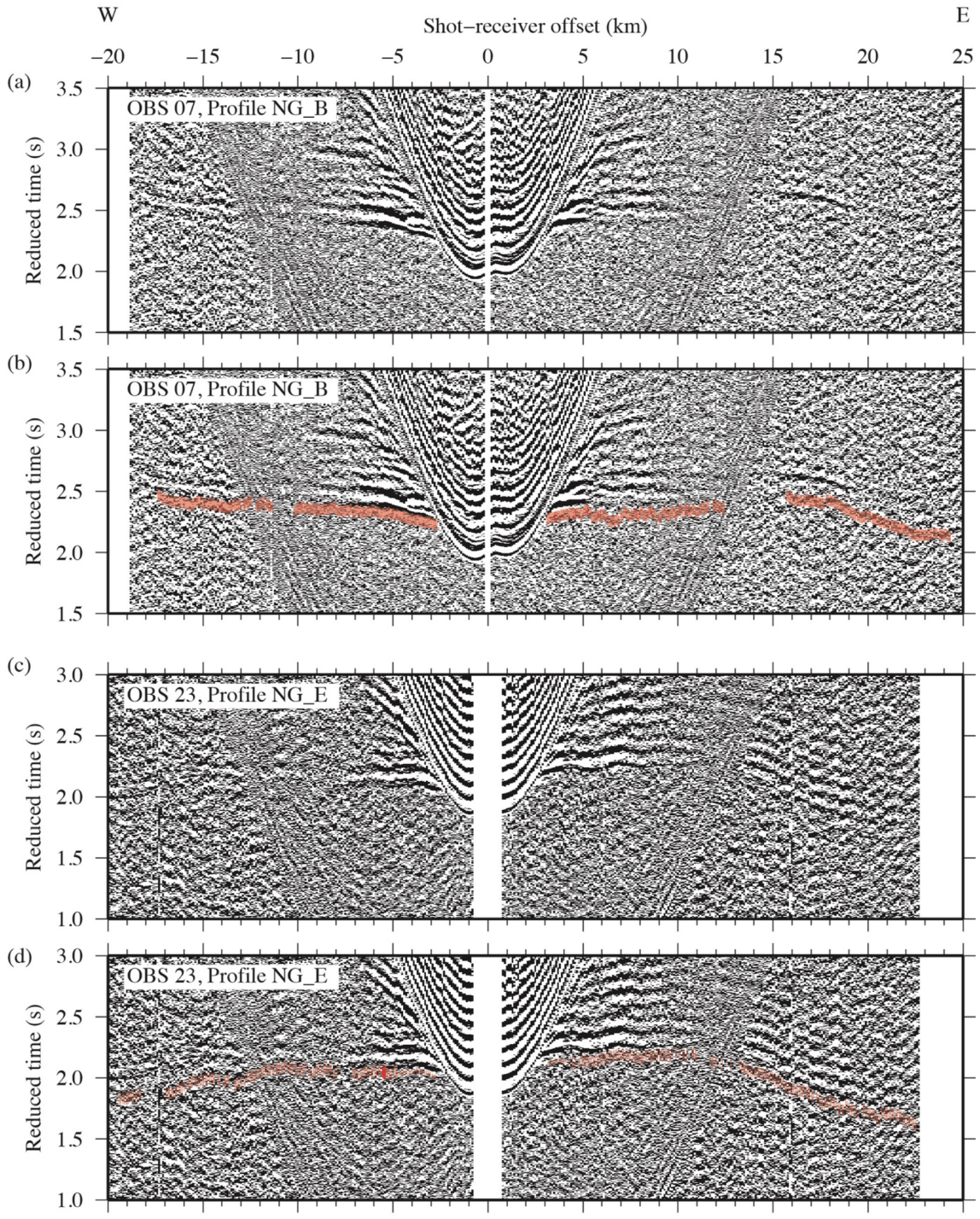

Figure 4. Example OBS hydrophone record sections, displayed using a minimum phase bandpass filter (1–4–88–120Hz) and a reduction velocity of 6 km s^{-1}. (a) OBS 07, Profile NG_B, which runs along the ridge axis with (b) traveltime picks annotated, where bar height corresponds to the assigned pick uncertainty (Table 1). (c) and (d) OBS 23, Profile NG_E, which is oriented ridge-parallel, off-axis to the south. (e) and (f) OBS 14, Profile NG_G, oriented across axis and intersecting (a) and (b).

velocity–depth structure as our initial starting point (Wilson *et al.* 2019), the vertical resolution of our *inversion model* is as good as that model, at 1.5 km, since that is larger than the inversion vertical cell size adopted here.

As part of resolution testing a set of synthetic traveltimes was calculated for the perturbed model and Gaussian noise added, scaled according to the pick uncertainties. These synthetic picks were then inverted, using the same parametrization used to achieve the *inversion model*, and using that model as the starting point. Where ray coverage density is sufficient to resolve model features, the output checkerboard should match the input pattern (Fig. 7a). The resolvability of particular length scales within a model is quantified by the semblance (Fig. 7a; Zelt 1999), which we calculate using an operator radius equal to the input anomaly size. We adopted Zelt's

(1999) semblance threshold of 0.7 to indicate where we consider the model to be well resolved. Rotation of the checkerboard pattern through 45° (Fig. 7b), together with lateral phase shifts of 0.5 times the checkerboard pattern cell size for both rotated and unrotated patterns, were also applied to appraise the effects of checkerboard edge geometry and ray path orientation dependence. Consequently, we tested eight unique checkerboard patterns.

In general, resolution is poorer for the rotated checkerboard patterns (Fig. 7d), rarely exceeding a semblance of ∼0.75, compared to the unrotated patterns (Fig. 7c) which commonly display a semblance of 0.9–1.0 beneath the OBS array. This trend is considered most likely a direct consequence of the grid-like acquisition geometry. Therefore, we averaged the results of all patterns in order to eliminate any orientation bias (Fig. 7e).

Resolution testing indicates that, for 0.5 km vertical (Z) inversion cells, an overall mean semblance of >0.7 is consistently observed to model depths of at least ∼2.5 km b.s.f. (Z = 5.5 km; Fig. 7e). For vertical cell sizes smaller than this (e.g. 0.2 km; Fig. 7f), tests indicate failure to consistently exceed the 0.7 semblance threshold at model depths of Z > 5 km beneath the extent of the OBS array, although a threshold of 0.6 is consistently exceeded. The results of checkerboard testing indicate that, at best, the limit of lateral resolution of our model is 3 × 3 km, while recovery is optimal at a vertical inversion cell size of 0.5 km.

5 MODEL DESCRIPTION

Our *inversion model* shows a variable *P*-wave velocity structure in the upper crust both across and along the CRR ridge axis. Three vertical slices (two orientated across axis and one along axis; Fig. 5) and three horizontal slices (constant depth within the model; Fig. 6) through this model are used to demonstrate its main features. In addition, 1-D velocity–depth profiles at various locations within the study area (Fig. 8) are used to better understand their significance and context with respect to processes occurring at spreading ridges in general.

5.1 'Background' crustal structure

Due to the inherently smooth and interface-free nature of inversion models, and the limited constraint on vertical velocity structure in the uppermost ∼0.5–0.8 km of the crust, we cannot directly determine the 2A/2B transition between extrusive pillow lavas and intrusive dykes. Wilson *et al.*'s (2019) model for Profile SAP_B provides a better constraint on the uppermost crustal structure, and showed this transition to occur at ∼0.6 km b.s.f.. However, at ∼2 km below seafloor, within the *P*-wave velocity range of ∼6.3–6.5 km s^{-1}, we observe a transition from higher to lower vertical velocity gradient (Fig. 8a). We interpret this feature as the layer 2B/3 transition (dykes/gabbro), with its depth consistent with global average oceanic crustal compilations (e.g. White *et al.* 1992) and with the co-incident across-axis 2-D SAP_B inversion model (Wilson *et al.* 2019; Fig. 5f). Off-axis, 1-D vertical velocity–depth profiles (Fig. 8b) suggest that layer 2 velocities to ∼2 km b.s.f. may be up to ∼0.2–0.3 km s^{-1} faster than at the ridge axis (Fig. 8d), suggesting that:

(i) the axial magmatic system is hotter than the off-axis crust and/or

(ii) the higher velocity observed off-axis relates to crustal ageing due to infilling of the layer 2 primary porosity as a result of hydrothermal circulation and mineral precipitation (Lowell *et al.* 1993).

Of these interpretations we prefer the former, since the 'crustal ageing' process should occur over greater spatial and, hence, temporal scales than 10 km (equivalent to ∼350 000 yr at the CRR).

Along-axis (Y = 30 km; Fig. 5e), higher velocities are observed in the region beneath the bathymetric dome (between X = 15–25 km). However, it is not clear whether this is a robust feature of the data set or an inversion artefact, perhaps associated with the adjacent lower velocity zone. If real, then its location conflicts with evidence which suggests that this part of the ridge axis is currently better supplied with magma (e.g. Buck *et al.* 1997; Haughton *et al.* 2018), unless some process is acting to increase the velocity that may be related to the presence of an active hydrothermal circulation system which both cools the ridge axis and 'freezes' any axial magma lens (Lowell *et al.* 2020), and infills the intrinsic upper crustal porosity (e.g. Vera *et al.* 1990; Detrick *et al.* 1994; Christeson *et al.* 2007).

5.2 Axial magma lens

The location of the AML (Fig. 3; Buck *et al.* 1997), at 1.2–1.4 s TWTT below the seafloor reflection, corresponds to a depth within the crust of ∼3.5 km, based on an average upper crustal velocity of 5 km s^{-1} (Lowell *et al.* 2020). This places this feature below the maximum depth to which our model samples and resolves the crustal velocity structure at the CRR. Furthermore, the waveform modelling determination of AML thickness of ∼100 m (Lowell *et al.* 2020), is less than the best-case vertical resolution of the *inversion model*, even if it were within the depth range of the model space that is sampled by rays. The *inversion model* cannot, therefore, by itself make any direct observations of the nature of the AML.

5.3 Low velocity zone

When viewed in horizontal slices, a ∼10 × 5 km region of reduced *P*-wave velocity, relative to the surrounding ridge axis, is observed beneath the OSC that is elliptical in shape and elongate along axis (Fig 6). This region is also observed as a broad zone below the ∼5 km s^{-1} contour, with an along axis length of ∼10–15 km (Fig. 5e). In the north–south oriented (across axis) profile, at model X = 30 km, this feature appears as a narrower zone, ∼5 km wide, consistent with the elliptical footprint within the constant depth slices (Fig. 5d). Checkerboard testing of the *inversion model* (Fig. 8) indicates that this feature should be well within the lateral resolution, having size greater than 3 × 3 km.

Above Z = 3.8 km/∼0.8 km b.s.f., vertical model slices show little evidence of a low velocity zone (LVZ), with velocity contours appearing either flat or mirroring the seabed bathymetry (Figs 5c and d), while the 1-D velocity–depth structure is similar to that of the ridge axis ∼10 km to the west (Fig. 8e). This observation may, in part, be due to the relative lack of constraint at the shallowest depths in the model. Alternatively, this may simply reflect the generally more porous structure of the uppermost part of the oceanic crust (e.g. Houtz & Ewing 1976; Christeson *et al.* 1992), such that the processes involved in the formation of the LVZ modify the velocity–depth structure below the resolution of the data and/or inversion approach applied here.

Below Z = 3.8 km, the velocity in the vicinity of the LVZ begins to decrease relative to the background ridge axis structure, by up to a maximum of ∼0.4–0.5 km s^{-1} at 2 km b.s.f. (Fig. 8e). Observed in plan view (Figs 6a–c and 9a), the LVZ can still be observed at

Table 1. Summary of traveltime pick uncertainties, showing the number of picks for each assigned traveltime uncertainty used for primary inversion, ray coverage and resolution analysis, and the investigation of the structure of the AML.

Pick uncertainty	15 ms	20 ms	30 ms	40 ms	45 ms	Total
Primary inversion		1348			67 144	68 492
LVZ investigation	1348		24 437	42 707		68 492

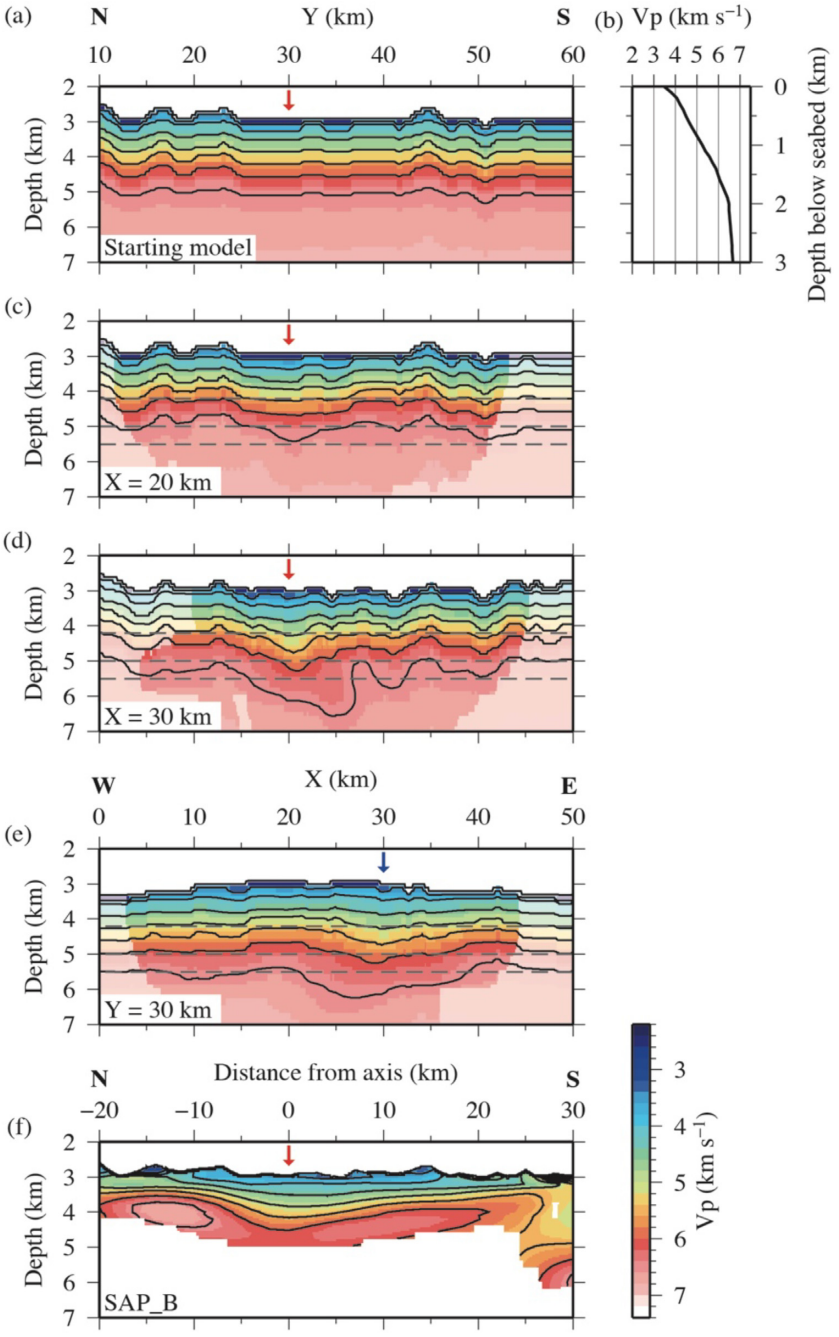

Figure 5. Starting model and modelling results. (a) 2-D vertical slice through the starting model at $X = 20$ km. (b) 1-D vertical velocity-depth profile at the ridge axis derived from a 2-D inversion of OBS data along SAP_B (Wilson *et al.* 2019). This was applied below bathymetry to generate starting model shown in (a). (c–e) Vertical model slices through the *inversion model* resulting from traveltime inversion using the starting model in (a) and the parameters in Table 2. Slices are taken (c) N–S through the region where the AML has been observed at the ridge axis, co-incident with Profile SAP_B, (d) N–S across the OSC, and (e) E–W along the ridge axis. (f) Ridge axis structure from 2-D inversion of OBS data along SAP_B (Wilson *et al.* 2019) for comparison. Red arrows in N–S oriented plots indicate the location of the ridge axis. Blue arrow in (e) marks the OSC. Models are masked by illumination to show areas constrained ray coverage. Contours are shown at 0.5 km s^{-1} intervals between 3.5 and 6.5 km s^{-1}. Dashed horizontal grey lines locate depth slices in Fig. 6.

Table 2. Summary of parameters used for inversion. The values given for the horizontal and vertical inversion cell sizes are for the preferred *inversion model* shown in Figs 5 and 6.

Inversion parameter	Value
sz	0.125
Alpha	0.95
Lambda0	100
Lambda reduction factor	1.414
Inversion cell—horizontal	0.5 km
Inversion cell—vertical	0.5 km

$Z = 5.5$ km, near the base of the well sampled and resolved part of the *inversion model*, while the 1-D velocity–depth profile through the LVZ shows reduced velocities to ∼4 km b.s.f., penetrating below the base of the resolved part of the model (Fig. 7e). We cannot, therefore, definitively determine the maximum depth to which the LVZ extends.

The LVZ is characterized by a slower *P*-wave velocity extending deeper into the model. The largest velocity differences between the LVZ and the background ridge axis structure occur shallower than ∼2.3 km b.s.f. ($Z = 5.3$ km), and are particularly evident in enlarged depth-slice views of the LVZ, which show this feature to be more prominent at $Z = 5.0$ km than at $Z = 5.5$ km (Fig. 9a). The total observed depth extent of the LVZ place it predominantly within the sheeted dyke sequence of layer 2B.

The lateral location of the LVZ coincides with the bathymetric expression of the OSC (Figs 2a, 6 and 9). Consequently, we interpret the low velocity anomaly to reflect enhanced tectonism between ridge segment tips. This results in increased fracturing and/or higher porosity and, hence, a decrease in velocity (Weekly *et al.* 2014). Lower model ray coverage to the east of the LVZ (Figs 6d–f) means that the velocity structure beneath the eastern limb is less well constrained than the western limb. The eastward extent of the LVZ cannot, therefore, be definitively determined. However, a lower velocity is observed to a distance of up to 10 km east of the OSC (Figs 6b, c and 9a, b). With increasing depth though, the slowest *P*-wave velocity appears to lie predominantly beneath the western ridge tip.

In an attempt to better constrain the lateral location and vertical depth and extent of the LVZ, the inversion was repeated with an 'at absolute best' set of traveltime picks, where an alternative set of smaller uncertainty values were assigned to picks at intermediate shot-receiver offset distances (Table 1). The result of this inversion (Fig. 9b) shows the LVZ to display a similar overall footprint to the *inversion model*, of ∼10–15 × 5 km, with an even lower *P*-wave velocity focused into a narrow zone beneath the western ridge tip. Relative to the 'background' ridge-axis structure, the maximum velocity anomaly associated with the LVZ using these pick uncertainties is ∼0.8 km s^{-1} (Fig. 9c) over a depth range of ∼1.0–2.5 km within the crust, ∼0.3 km s^{-1} slower than in the *inversion model* (Figs 5c–e, 6a–c, 8c, e and 9a). The results of this inversion are consistent with our interpretation that the low velocity anomaly is a manifestation of the increased porosity generated by fracturing associated with the OSC.

6 POTENTIAL FIELD DATA

To further our understanding of the magmatic and tectonic processes at the CRR, we analysed the gravity anomaly in two ways. The first, using the ship-derived free-air anomaly (FAA), allows us to appraise if the *inversion model* is a robust solution, potentially revealing features below its resolution or extent of ray coverage, particularly within the lower crust and/or upper mantle. It also provides some constraint on crustal thickness variation. To create the ship-derived FAA, cross-over analysis (Wessel 2010) was performed on the data acquired along each profile within the NG to remove systematic errors, and a datum shift was applied to equate the ship data to the global satellite-derived FAA (Sandwell *et al.* 2014; Fig. 10b). The resulting ship-derived FAA is shown in Fig. 11(b). The second approach, using the satellite-derived FAA, allows us to set our observations within the context of the entire CRR ridge system. In particular, we are able to extend our understanding of the ridge axis structure beyond 5 km to the east of the OSC, where there is no seismic constraint.

6.1 Density models

To construct the initial 2-D density models, the *inversion model* was sampled along two vertical profiles running north-south through the AML ($X = 20$ km) and OSC ($X = 30$ km). Using the 4.55 and 6.25 km s^{-1} velocity contours to represent the layer 2A/2B and 2B/3 boundaries, polygons representing layer 2A and 2B were defined, to which constant densities of 2450 and 2700 kg m^{-3} were assigned respectively, based on the velocity–density relationship of Carlson & Raskin (1984). To define the base of the crust in each initial model, which lies below the base of the resolved region of the *inversion model*, we used a constant crustal thickness of 6 km, consistent with the spreading rate (White *et al.* 1992; Bown & White 1994) and that used in the MBA calculations of Wilson *et al.* (2019). Layer 3 was assigned a density of 2950 kg m^{-3}, the mantle 3310 kg m^{-3} and the water column 1035 kg m^{-3}. Model edge effects were prevented by extending the density structure for 1000 km beyond the model limits. The FAA associated with each density model was then calculated using *grav2d*, based on the method of Talwani *et al.* (1959).

6.2 Across-axis profile through the AML

The north–south profile through the grid at $X = 20$ km model offset (Figs 11c–f), coinciding with the location of the AML (Buck *et al.* 1997) and Profile SAP_B (Wilson *et al.* 2019), shows that observed FAA can be entirely explained by the seismically resolved layer 2 structure. No additional variation in crustal thickness and/or density in the lower crust (layer 3) or mantle, where the *inversion model* has limited-to-no constraint, is required to result in a good fit to the observed data. This supports observations which suggest that the AML itself is a small feature (Buck *et al.* 1997; Lowell *et al.* 2020), too small to have any manifestation in the 2-D density model which traverses it. However, any low density and, hence, low velocity zone beneath it should be observable if spreading is currently magmatically supported. Our *AML density model* suggests that there is no significant across-axis density anomaly arising from hotter thermal conditions associated with a magma source region, which may support the hypothesis that the magma supply to the CRR AML is periodic and/or weak. Alternatively, it could also be the case that this feature has an across-axis scale much longer than the ±20 km from the ridge axis over which the ship-based FAA was measured. However, the latter possibility is not supported by the lower lateral resolution satellite-derived data (Fig. 10).

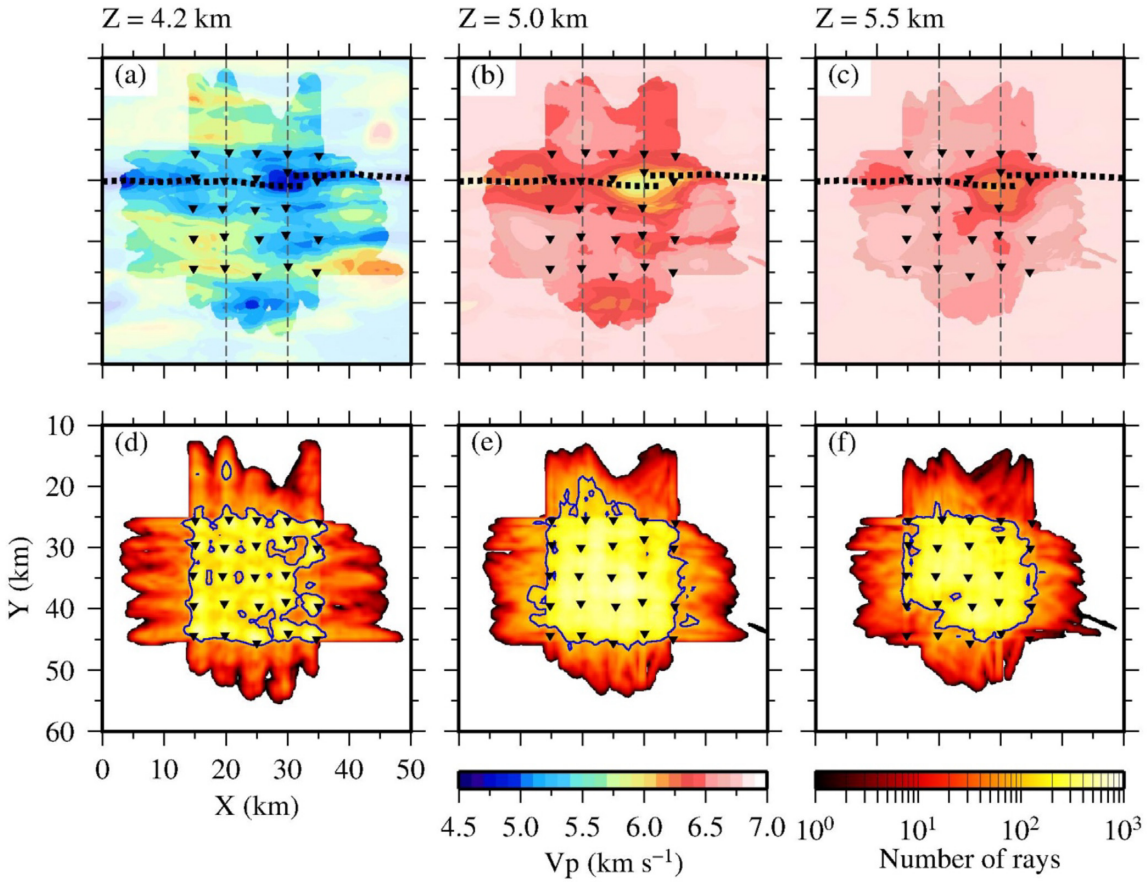

Figure 6. *Inversion model* derived with 0.5-km-lateral and 0.5-km-vertical inversion cells. Horizontal (constant model depth) slices at: (a) $Z = 4.2$ km (~1.2 km b.s.f.); (b) Z = 5.0 km (~2.0 km b.s.f.) and (c) Z = 5.5 km (~2.5 km b.s.f.). Illumination masking shows the extent of model ray coverage and the dotted line shows the centre line of the west and east CRR ridge segments. Inverted black triangles show OBS locations. Dashed grey lines show locations of vertical slices shown in Figs 5(c)–(d). (d)–(f) Corresponding ray coverage. Blue line delimits inverse cells with more than 100 ray hits.

6.3 Across-axis profile through the OSC

In contrast, a constant crustal thickness and density model for the north–south profile ($X = 30$ km) which traverses the OSC and associated LVZ at the ridge axis (Fig. 11i) does not produce a FAA that fits the observed (Figs 11g, h). Negative misfits (modelled < observed) between 24–44 km and 48–56 km distance along profile suggest that these regions are underlain by either a thinner crust or more dense crust and/or mantle compared to the OSC at the ridge axis. Since the *inversion model* has lower velocity beneath the OSC to depths of ~2.5 km b.s.f. (Z = 5.5 km; Figs 6a–c, 8e), it would be inconsistent to model these features with localized higher density blocks. We thus suggest that the mismatch is best explained by a thinner crust on-axis than off-axis.

We test this hypothesis by adjusting the depth of the base of layer 3 (Fig. 11j), and find that the degree of thinning required, assuming no lateral changes in density, is ~1.0–1.6 km. If this crustal thinning is facilitated by faulting this may result in the formation of fluid pathways throughout the crust which may allow fluids to infiltrate the uppermost mantle, causing alteration and lowering of its density. Consequently, there is a trade-off between density decrease and increased thinning. Our *OSC density model* (Fig. 11k) shows that, for a 110 kg m^{-3} lower density mantle within the thinned region, layer 3 must further reduce in thickness by another 0.5 km relative to the constant density case, to produce a fit to the FAA within error.

Comparing the locations of misfit and corresponding model adjustments with the across-axis bathymetry (Fig. 11l), we find that they coincide with variations from shallower to deeper off-axis seafloor. The latter locations are interpreted by Wilson *et al.* (2019) to reflect periods of increased tectonic stretching. The regions of crustal thinning are also not symmetrically distributed either side of the ridge axis, with the central region beneath the OSC being offset to the south, and the flanking regions being ~15–20 km off-axis to the north and 18–24 km to the south. This observation reflects the observed asymmetry in the spreading rates for the two ridge flanks (Wilson & Hey 1995; Wilson *et al.* 2019).

6.4 Regional features

To place our observations within the NG in context of the CRR segment as a whole, we use the GEBCO (2008) bathymetry (Fig. 10a), the Sandwell *et al.* (2014) FAA (Fig. 10b) and the MBA (Fig. 10c) and residual MBA (RMBA; Fig. 10d) of Wilson *et al.* (2019). A datum was subtracted from the RMBA to produce the residual RMBA (rRMBA; Fig. 10e), with values distributed around zero. The resulting rRMBA represents deviations in structure from the reference crustal thickness and density used for the reduction. Thus, higher or more positive values imply that either the crust is thinner than the 6 km reference thickness used in the calculation, or that the crust and/or mantle are denser than the reference values, or a combination of these, with the opposite true for lower/more negative values.

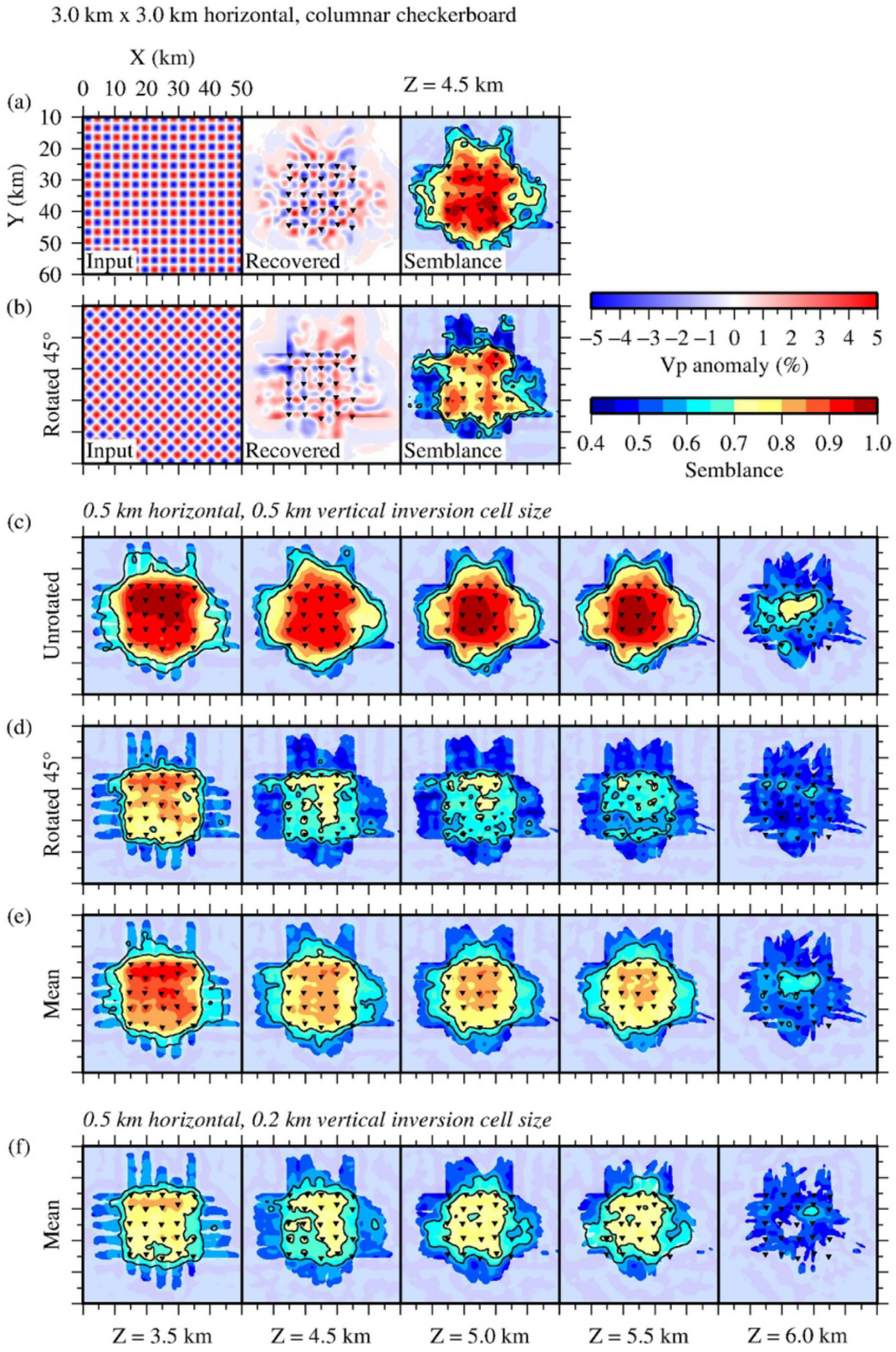

Figure 7. Resolution analysis of the *inversion model* using a 3 × 3 km checkerboard. (a) Input to (left-hand panel) and resultant pattern after (centre panel) checkerboard testing, and resulting semblance (right-hand panel) at $Z = 4.5$ km (∼1.5 km b.s.f.). (b) As a), with a 45° rotation applied to input pattern. Averaged semblance of four pattern phase shifts to the (c) unrotated and (d) rotated 45° input checkerboard patterns and (e) for all eight unique input test patterns. (f) Mean semblance for eight unique input test patterns for the 0.5 km horizontal, 0.2 km vertical inverse cell size parametrization. Depths (Z) of model slices are annotated. The 0.6 and 0.7 semblance contours are shown in black.

We observe a trend in the rRMBA from lower/negative values adjacent to the Ecuador Fracture Zone in the west, to higher/positive values towards the Panama Fracture Zone in the east. The transition between these regions approximately coincides in longitude with the OSC, to the east of which the deeper ridge axis is inferred to reflect a weaker magma supply. The rRMBA further supports this hypothesis, indicating either colder and, hence, denser crust and/or mantle material, or an increased prominence of tectonic stretching that thins the crust. This along-ridge trend is also observed to extend

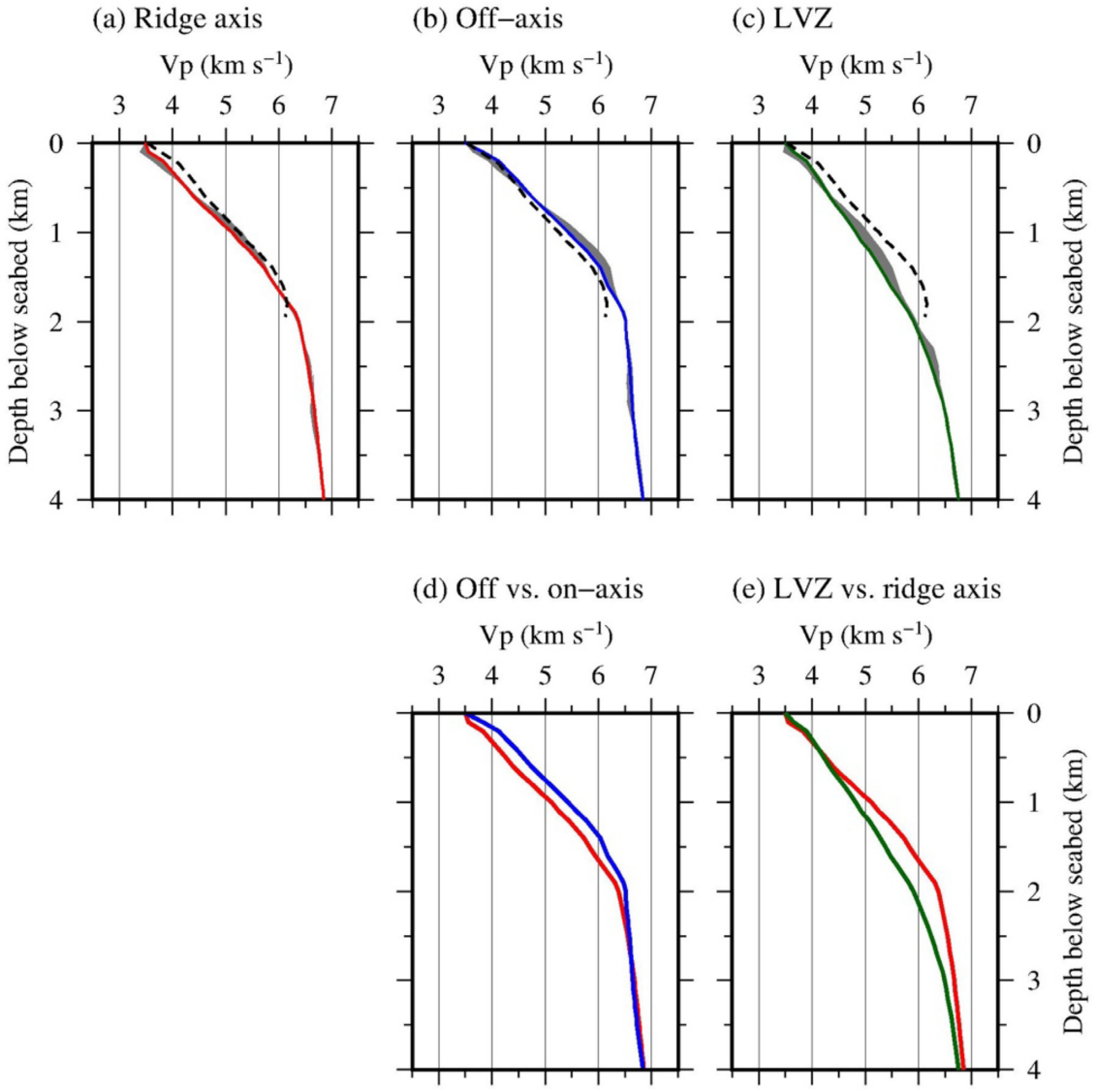

Figure 8. 1-D vertical velocity–depth profiles through the *inversion model*. (a) Velocity–depth profiles at the ridge axis, away from the LVZ (X = 20 km, *Y* = 30 km model space), coinciding with SAP_B. Red line is the *inversion model.* Grey envelope represents the range of resulting structures from all tested inversion parametrizations. Black dashed line is the Wilson *et al.* (2019) 2-D OBS inversion velocity–depth structure at the ridge axis. (b) Off-axis, 10 km to the south (*X* = 20 km, *Y* = 40 km; blue line). (c) At the location of maximum LVZ amplitude (*X* = 29 km, *Y* = 31 km; green line). (d) Comparison between off- and on-axis velocity–depth profiles through the *inversion model*. Line colours correspond to the model locations shown in (a) & (b). (e) Comparison between LVZ and ridge axis profiles.

for ∼80–100 km off-axis (Fig. 10e), corresponding to crustal ages of up to ∼3 Ma (Wilson & Hey 1995; Wilson *et al.* 2019).

Seismic attenuation studies (e.g. Vargas *et al.* 2018), using both onshore and offshore recordings of earthquakes, suggest that the Panama Fracture Zone (which bounds the CRR to the east; Fig 1a) coincides with a significant thermal anomaly in the lithosphere, extending to at least ∼30 km depth. We suggest that this feature may effectively 'chill' the adjacent lithosphere to the west, with the extent of this effect being shown by the along-segment transition in rRMBA values from positive to negative.

7 DISCUSSION

7.1 CRR ridge structure, magma supply and spreading characteristics

The present mean axial depth of the CRR is ∼3 km, deeper than might be expected from its spreading rate (∼65 mm yr^{-1} FSR; e.g. Mendel *et al.* 2003; Dannowski *et al.* 2010), and may suggest that the ridge system is currently spreading in a manner similar to a slower, MAR-type end-member. Changes in the bathymetric profile along segment, from a bathymetric dome to the west of the OSC to a deeper axial valley to the east (Fig. 2b), in turn, suggest variability in along axis magma delivery. However, axial depth is not necessarily a direct indicator of ridge equilibrium state and, instead, could reflect episodic periods of magmatic spreading, or the dynamic (shorter

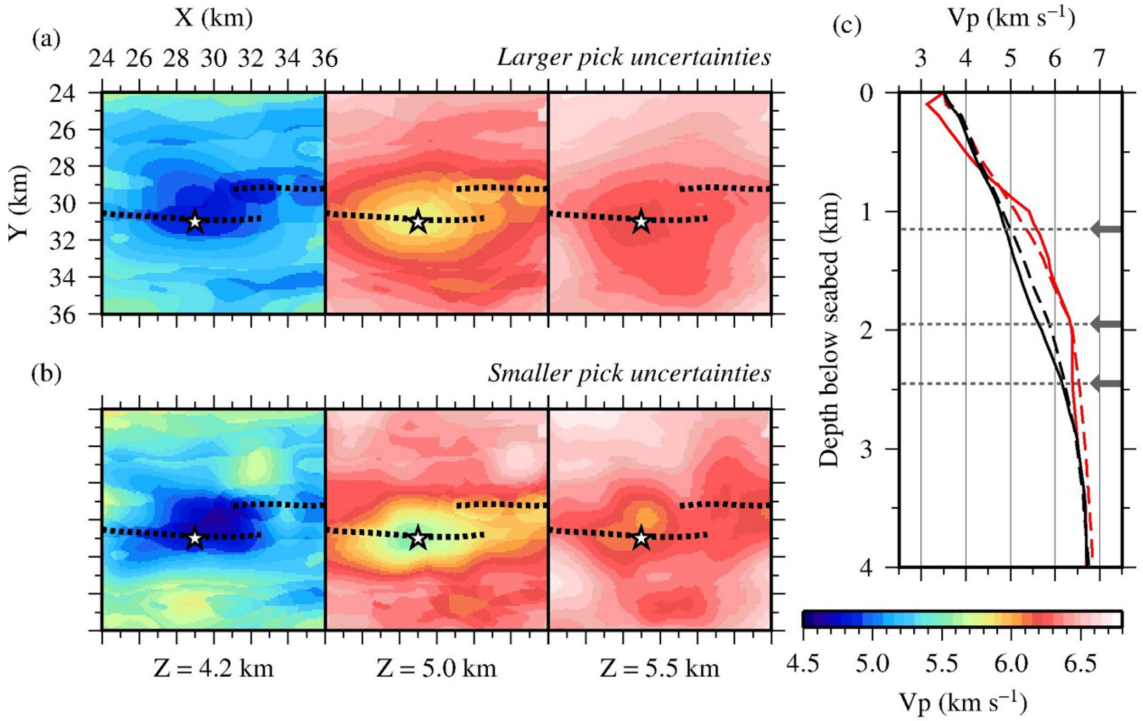

Figure 9. Constraints on *inversion model* anomaly variation. (a) LVZ at Z = 4.2, 5.0 and 5.5 km. Black dashed line indicates centre line of each CRR ridge segment. Star at $X = 29$ km, $Y = 31$ km corresponds to the location where 1-D profiles in (c) and Fig. 8(c) are sampled. (b) Corresponding LVZ structure for the model generated using 'at-best' pick uncertainties, showing the LVZ to be concentrated beneath the western spreading limb (see text). (c) 1-D velocity-depth profiles at the ridge axis ($X = 20$ km, $Y = 30$ km; red) and through the OSC LVZ ($X = 29$ km, $Y = 31$ km; black). Solid lines correspond to the 'at-best' pick uncertainty model, and dashed lines to the *inversion model*. Grey arrows and dashed lines approximately show the depths of the constant depth slices (a–b).

time scale) effects of magmatic intrusion and its related faulting and fracturing (e.g. Carbotte *et al.* 2006).

Observation of an axial magma lens (Buck *et al.* 1997), which may persist over or be resupplied within an ∼20-yr timescale (Lowell *et al.* 2020), does not necessarily conflict with an interpretation that a slower end-member style of spreading is currently ongoing at the CRR. In tandem with the observation of a water column hydrothermal plume at the ridge axis, thermal modelling (Lowell *et al.* 2020) suggests that the magmatic input to the AML may be relatively small and episodic, rather than continuous and well supported over time, as is the case for EPR-type ridge systems. This conclusion is further supported by the lack of evidence from potential field modelling for a significant lower crustal or upper mantle heat anomaly, which would be expected if the magma supply is robust. Instead, our across-axis FAA modelling shows that the observed anomaly can be explained entirely by the upper crustal (layer 2) structure.

Off axis, the basement fabric and crustal velocity structure both record changes in the style of spreading. Wilson *et al.* (2019) suggest that the CRR may exist at a tipping point, where the supply of magma to the ridge is sensitive to small fluctuations in the full spreading rate. As such, there may be periods of more well-supplied and, hence, magma-rich spreading, which alternate with periods where plate separation is primarily accommodated by tectonic stretching and faulting over million-year timescales, where the balance between the two is dictated by fine-scale changes in the spreading rate, as small as 3–5 mm yr^{-1}.

7.2 OSC stability and evolution

The overlap (∼2.5 km) and offset (∼1.5 km) of the CRR OSC result in an overlap to offset ratio of ∼1.6:1, which is relatively small compared to that of the well-established OSCs found at the EPR and JdFR at 3:1 (e.g. Macdonald & Fox 1983; Canales *et al.* 2003, 2005; Weekly *et al.* 2014). Consequently, the OSC at the CRR may be interpreted to be at a relatively nascent stage within its lifespan. However, despite this, the CRR OSC footprint does have a direct correlation with the velocity anomaly structure in the upper and middle parts of the crust, with a 0.5–0.8 km s^{-1} reduced *P*-wave velocity extending to ≥2.5 km b.s.f. We interpret this reduced velocity as reflecting an increase in porosity due to fracturing associated with the progressive formation of the OSC, a process which has been shown to result in porosity increases of ∼10 per cent (Christeson *et al.* 1997).

Our observation is similar to velocity anomalies associated with other magmatically active mid-segment regions. For example, the 9°03′N OSC at the EPR (Tong *et al.* 2002) displays a localized velocity decrease of ∼0.3–0.5 km s^{-1}, extending to depths of up to ∼2 km b.s.f. At the much larger (30 km overlap, 10 km offset) Endeavour-West Valley and Cobb OSCs, at ∼48°N on the JdFR, *P*-wave velocity is up to 1 km s^{-1} slower than along the adjacent ridge segments (Weekly *et al.* 2014), although a component of this is attributed to velocity increase due to porosity infilling in the mid-segment regions as a result of hydrothermal circulation and mineral precipitation (Lowell *et al.* 1993).

Tong *et al.* (2003) propose a dynamic magma supply model for OSCs, in which variations in the magma budget of the offset ridge segments may affect if and how the discontinuity migrates along-ridge. Where magma supply is balanced either side of the

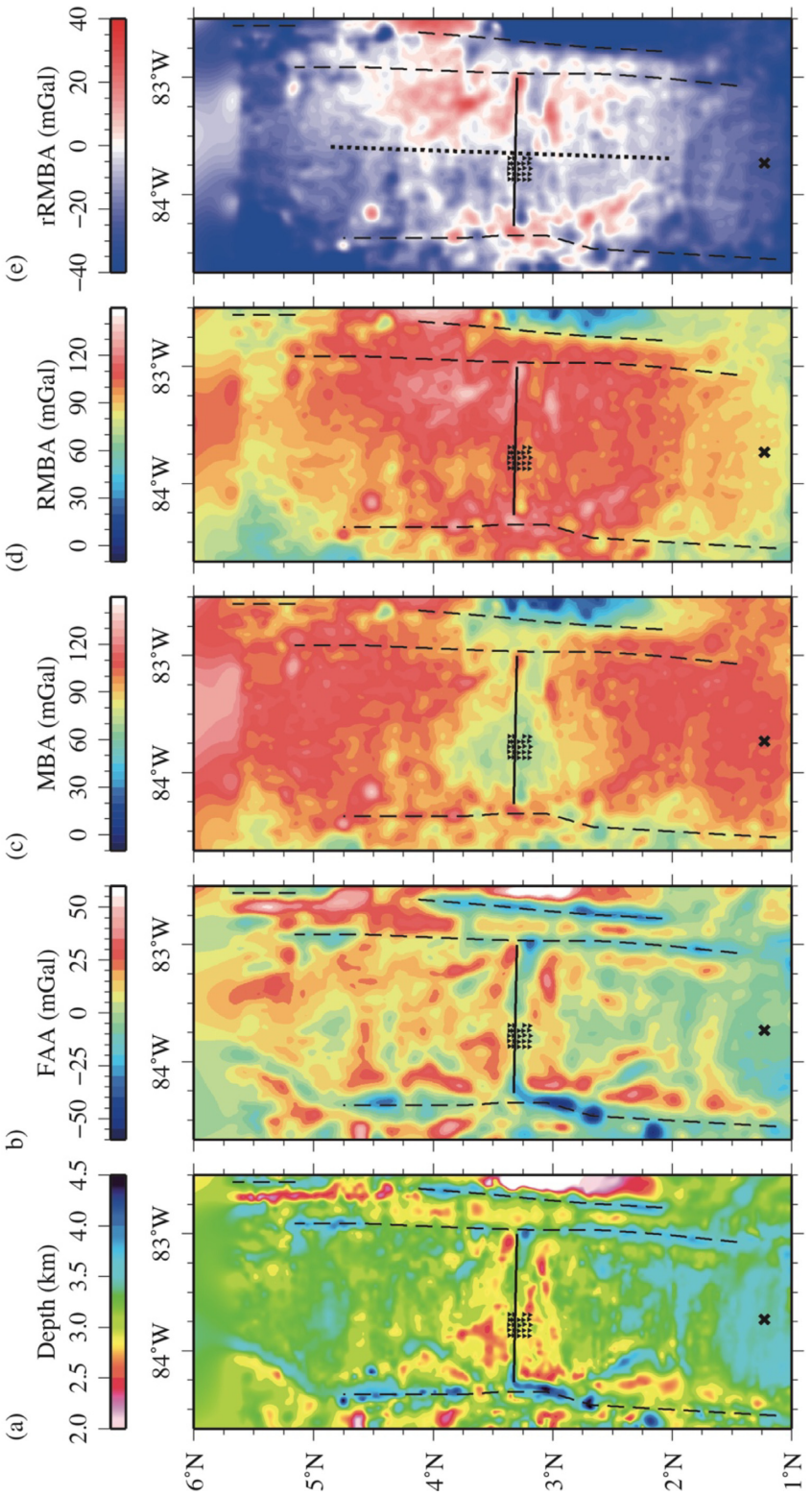

Figure 10. CRR segment-scale potential field data, extending ∼250 km to the north and south of the ridge axis. (a) GEBCO (2008) bathymetry. (b) Satellite-derived FAA (Sandwell *et al.* 2014). (c) MBA, calculated using a crustal thickness of 6 km and densities of 1035, 2700 and 3300 kg m^{-3} for the water column, crust and mantle respectively. (d) RMBA, calculated using an average half-spreading rate for both ridge flanks of 33 mm yr^{-1}. (e) rRMBA, calculated by applying a datum shift to (d) to distribute anomalies around zero for relative polarity analysis. Solid black lines indicate the location of the ridge axis. Dashed black lines are the segment-bounding fracture zones. Black inverted triangles show OBS locations. Cross indicates the location of borehole 504B. Dotted black line in (e) shows the location of the change from lower to higher rRMBA from east to west, lying ∼8–10 km west of the OSC at the ridge axis.

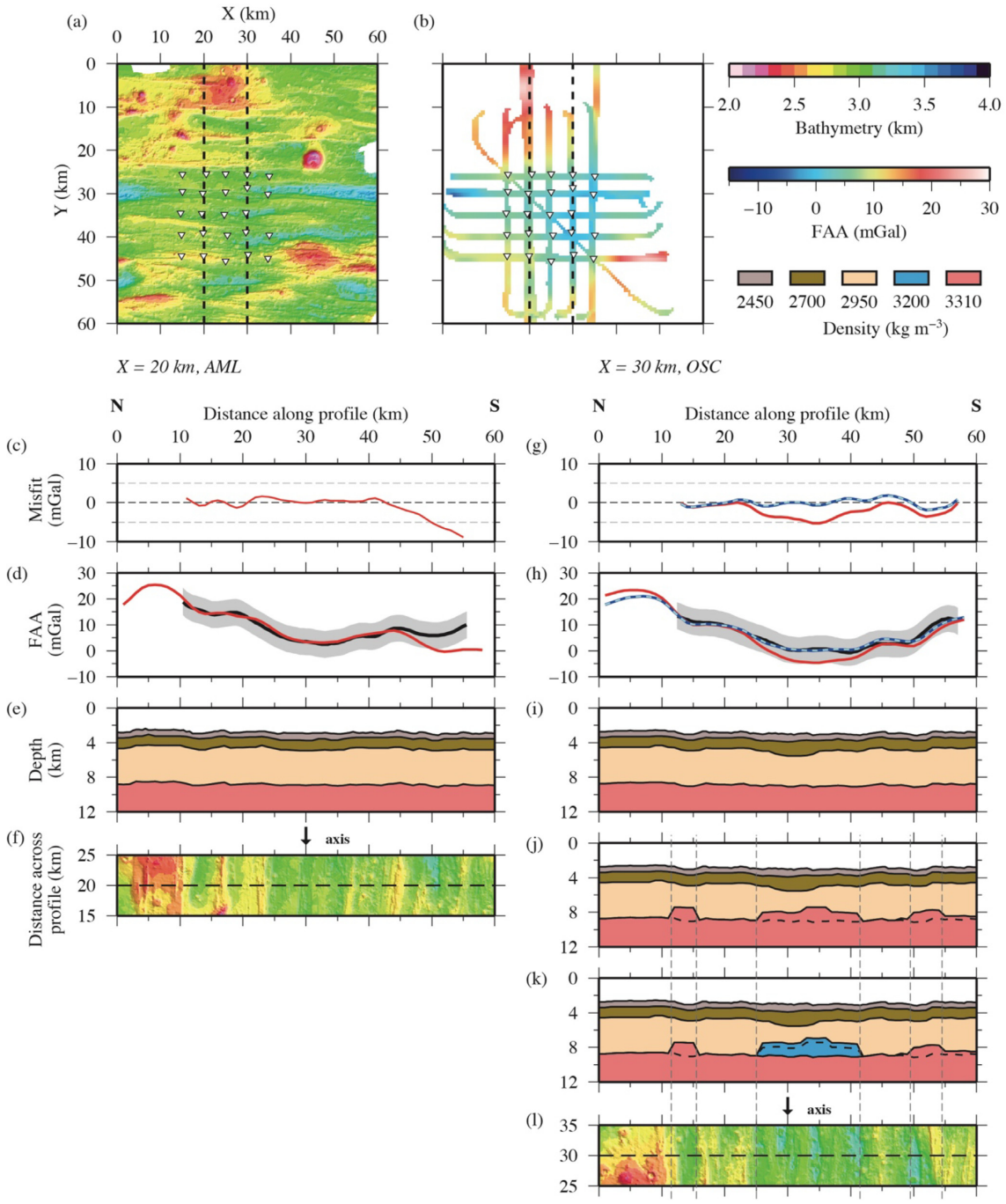

Figure 11. 2-D gravity modelling. (a) Ship-acquired swath bathymetry data. Inverted triangles show OBS locations. Black dashed lines correspond to profile locations shown in (c–f) and (g–l). (b) Cross-over corrected and gridded JC114 ship-acquired FAA. Left-hand panel: AML gravity modelling ($X = 20$ km). (c) Misfit between observed and modelled FAA. (d) Observed (black) and modelled (red) FAA corresponding to the model shown in (e). Grey envelope shows the ±5 mGal error bound. (e) Crustal *AML density model*, derived using 4.55 and 6.25 km s^{-1} contours from the *inversion model,* a constant total thickness crust (6 km), and density from Carlson & Raskin (1984). (f) Ship-acquired bathymetry along modelled profile (black dashed line). Black arrow shows the location of ridge axis. Right-hand panel: OSC gravity modelling ($X = 30$ km). (g) Misfit between observed and modelled FAA as in (c). Line colours correspond to density models shown in (i–k): red—constant crustal thickness, (i); dark blue—variable thickness, constant density (j); light blue, dashed—variable thickness, variable density (k). (h) Observed (black) and modelled FAA, line colours correspond to models as in (g). (i) Constant crustal thickness block model. (j) Variable crustal thickness block model. Dashed black lines show crustal thickness variability relative to the model in (i). (k) *OSC density model* with variable crustal thickness and variable density. Dashed black lines show crustal thickness variation relative to the models in (i) and (j). (l) Ship-acquired bathymetry, as in (f). Dashed vertical lines through (j–l) show the correlation between variable crustal structure and bathymetry.

discontinuity, the OSC tends to remain at a stationary along-ridge position. However, where one limb is better supplied with magma, it will tend to propagate at the expense of the other, which will self-decapitate (Macdonald & Fox 1983; Macdonald *et al.* 1987).

The apparent LVZ focussing beneath the western ridge tip (Figs 9a and b) may suggest that this limb is currently undergoing a greater degree of tectonism, although the limitations of model ray coverage and resolution mean that it cannot definitively be determined how far east the LVZ extends away from the OSC. If tectonism is more active here, it would lead to the formation of open fractures that results in the observed decrease in the seismic velocity (Macdonald *et al.* 1988), despite the observation of an AML (Buck *et al.* 1997; Lowell *et al.* 2020) which suggests that this limb has a magma supply. In addition, both the degree of seismic attenuation (Vargas *et al.* 2018) and the potential field data analysed here also suggest that the CRR to the west of the OSC may have a more robust magma supply than to the east (Lowell *et al.* 2020), although there is limited shallow seismic crustal constraint on this. Microseismicity observations suggest that a high-temperature hydrothermal circulation system is active in the crust above the AML, whose cooling effect and open fracture pathways may also contribute to the lower P-wave velocity (Fig. 3b; Lowell *et al.* 2020).

At distances of up to ∼30 km from the ridge axis, swath bathymetry data identifies a series of axis-aligned basins between ∼12 and 15 km long, ∼3 km wide, and up to ∼300 m deep. These are interpreted as recording past ridge-axis discontinuities up to 1 Myr in age (Fig. 1, Haughton *et al.* 2018). Indicative 2-D gravity modelling (Figs 11j, k) suggests that these basins are underlain by thinner crust, which may be a result of increased tectonic stretching during formation of past ridge discontinuities. These basins do not resemble the V-shaped wakes observed at well-developed OSCs, such as the 9°03′N OSC of the EPR (Macdonald *et al.* 1984) and the 93°15′W OSC of the GSR (Canales *et al.* 1997), and do not show a significant lateral offset from the present along-ridge location of the OSC. This may suggest that ridge tip migration at the CRR is either slow or absent, likely as a consequence of an overall relatively weak magma supply to the ridge axis.

7.3 Hydrothermal exploitation of the fracture network

The pattern of microseismicity and observations of hydrothermal venting at the CRR (Fig. 3b; Lowell *et al.* 2020) suggest that its OSC may facilitate and focus fluid circulation. With the existing data it is not possible to unequivocally identify locations of outflow and recharge, although the single observation of a hydrothermal plume (Lowell *et al.* 2020) locates an at least transient expulsion of fluid from the system. Similar associations between microseismicity, axial magma systems, and observations of hydrothermal venting elsewhere (e.g. Wilcock *et al.* 2002; Dziak *et al.* 2007; van Ark *et al.* 2007; Tolstoy *et al.* 2008) have been interpreted as reflecting the action of hydraulic fracturing within the circulatory system.

As part of its formation, the crust adjacent to and below the OSC should undergo significant faulting and fracturing, increasing the crustal porosity and permeability, and resulting in the LVZ observed in the seismic velocity models. Therefore, this highly fractured region may provide a potential pathway for fluid ingress, which may enhance cooling of the magmatic system beneath. If that is the case, this may explain why the AML appears to terminate before it reaches the discontinuity (Fig. 3; Buck et al 1997), effectively being prevented from lateral flow by a cooling front.

Above the magma lens, as the hydrothermal fluids begin to cool, mineral precipitation may lead to infill of the intrinsic upper crustal porosity and permeability (Lowell *et al.* 1993, 2013) which would manifest as an increase in observed *P*-wave velocity in this region. Our modelling provides potential evidence that this process may be occurring, with *P*-wave velocity contours between 4.5 and 5.5 km s^{-1}, between 15 and 25 km along axis, being concentrated into a much narrower depth range than their equivalent elsewhere (Fig. 5).

7.4 Relationships between magma supply and ridge segmentation

Ridge axis depth (Fig. 2b) and volcanic morphology analysis (Haughton *et al.* 2018) both suggest that the ridge segment to the west of the OSC currently has an enhanced magma supply relative to the eastern segment. This conclusion is further supported by the rRMBA (Fig. 10e), which demonstrates a corresponding transition from lower/negative to higher/positive values along the ridge axis from west to east. This trend suggests that the segment to the east of the OSC is characterized by either a thinner crust, consistent with spreading accommodation through tectonic stretching under relatively magma-poor conditions, or that the crust and/or mantle is denser than that to the west. Both of these interpretations ultimately lead to an along ridge thermal anomaly and/or gradient, consistent with seismic attenuation studies that reveal a thermal anomaly within the lithosphere, delimited by the Panama Fracture Zone and bounding the CRR to the east (Vargas *et al.* 2018). The consequence is a 'chilling' of the warmer lithosphere immediately adjacent to the cooler.

The rRMBA variation along ridge is also observed to extend for ∼80–100 km off-axis, equivalent to up to ∼3 Myr (Wilson & Hey 1995; Wilson *et al.* 2019). Consequently, processes occurring at present may have been active for extended periods of time, either continuously or intermittently, as marked by a series of off-axis basins that Haughton *et al.* (2018) interpret as relics of previous non-transform discontinuities at the ridge axis. 2-D gravity modelling north-south across these features suggests that they are characterized by thinner crust than that formed away from the OSC (Figs 11j and k). Three of these features are seen to the south of the ridge-axis, at distances of ∼5, ∼10 and ∼20 km, and there are two similar features to the north at ∼5 and ∼15 km from the ridge. However, in the latter case, the north flank of the ridge appears to be overlain by lava flows, affecting our ability to map their locus of eruption and extent, and masking older spreading-related features. Based on the present-day CRR half-spreading rate, the off-axis distances of these basins suggest a periodicity in formation of ∼0.15–0.35 Myr.

7.5 Overview

When taken together, our models and observations suggest that the present-day OSC may exist because of a fundamental along ridge segment boundary whose inherited characteristics have persisted in the crust for at least ∼3 Myr. This feature presently represents the boundary between more magmatically robust (i.e. well supplied) spreading and magmatically episodic spreading, during which relatively short phases of magmatic accretion are interspersed by relatively long periods of tectonic stretching. The co-occurrence of the observed hydrothermal system at the CRR, together with the larger lithospheric scale temperature anomaly, suggests that the magmatic-tectonic processes at the CRR may be influenced by two integrated cooling mechanisms: one in the shallower crust, due to

enhanced hydrothermal circulation as a result of the magma heat source and the open cracks arising from tectonism; and the other extending throughout the lithosphere, arising from the juxtaposition of a cooler plate against a warmer. The OSC may, therefore, exist where it does due to that location along-segment being the limit of the cooling exerted by the colder plate to the east. In turn, the OSC itself opens more fractures/faults, allowing more fluid to flow and resulting in even more cooling, at least at upper crustal levels—a positive feedback loop.

Furthermore, the cooling effect of the hydrothermal system at the OSC presents a barrier to lateral magma flow along segment from west to east, thus further contributing to the increasingly magma-limited mode of spreading of the eastern segment. The absence of seismic constraint beyond ∼5 km to the east of the OSC, in addition to the 2-D nature of the acquisition of the MCS profiles, means that the presence or absence of an AML, either beneath the eastern ridge segment or the OSC itself cannot unequivocally be determined. However, our analysis of the potential field data suggests that the eastern ridge segment displays little evidence to support the presence of significant axial magma accumulations.

Therefore, when considered in the context of the observed off-axis variability in the dominant spreading mode (Wilson *et al.* 2019), the CRR may exist in a finely balanced state between magmatic accretion and tectonic spreading not only across axis but also along. These phases are turned on or off by long period (Myr), large scale (>10 s km) changes in the magma supply rate, which itself may be controlled by a range of external factors, including changes in the direction of plate motion and large-scale, pre-existing crustal and/or lithospheric heterogeneity.

8 CONCLUSIONS

Tomographic modelling of the OSCAR North Grid 3-D WA seismic data acquired at the Costa Rica Rift has revealed a *P*-wave seismic velocity anomaly low associated with an OSC-type non-transform discontinuity of the ridge axis. By combining this observation with other geophysical observations from the OSCAR project and previous experiments at the CRR, we draw the following conclusions:

1. The broad LVZ beneath the OSC, with dimensions of ∼10 × 5 km and a maximum velocity anomaly relative to the 'background' ridge axis crustal structure of ∼0.5–0.8 km s^{-1}, arises due to increased fracturing under enhanced tectonic stress, which increases the upper crustal bulk porosity and permeability. The apparent location of the LVZ maximum beneath the western ridge tip may suggest that this region is currently undergoing the higher degree of tectonic extension, associated with the evolution of the OSC.

2. The presence of a fluid circulation system at the CRR is supported by observations of hydrothermal plume activity and the location and temporal pattern of microseismic events, such that this system may exploit the open fracture/fault pathways which manifest as a low velocity zone beneath the ridge discontinuity. A hydrothermal system would cause rapid cooling of the ridge axis and any axial magma accumulations and, thus, may prevent eastward migration away from the more magma robust ridge segment to the west.

3. The Costa Rica Rift lies in a finely balanced state between episodic phases of magmatic accretion and tectonically-dominated spreading. It displays evidence for magmatic accretion ongoing at the ridge axis in the form of an AML. However, its dimensions, and the lack of evidence in crustal scale seismic and gravity models for a significant heat source, suggest that overall the magma supply is relatively weak.

4. The fine balance between alternating phases of magmatic accretion and tectonically dominated spreading at intermediate spreading ridges that we propose is recorded in the crustal morphology off-axis. Across-axis, variable spreading rate appears to control when the crustal formation process tips between the two end-member states. However, such variation between end-member spreading modes is also observed along axis, where it arises due to full-crustal or lithosphere scale structural and/or thermal heterogeneity as shown in the gravity models, and where it subsequently contributes to magmatic and/or tectonic segmentation of the ridge system.

ACKNOWLEDGEMENTS

This research was funded by the NERC Natural Environmental Research Council grants NE/I027010/1 and NE/I022957/2. We would like to thank all those involved in the planning and acquisition of data during research cruise JC114, including the officers, engineers and crew of the RRS James Cook, the scientific party and all seagoing NERC facility technicians and engineers. The NERC Ocean-Bottom Instrumentation Facility (Minshull *et al.* 2005) provided the OBSs and their technical support at sea. The MCS data were processed using Claritas™ and Seismic Unix (Cohen & Stockwell 2010). All figures were prepared using the Generic Mapping Tools (GMT–Wessel & Smith 1998). All data from cruise JC114 are archived at the NERC's British Oceanographic Data Centre, and the final accepted version of this paper is available through Durham Research Online (dro.dur.ac.uk). We thank the editor and reviewers for their positive and helpful comments which improved the clarity of this paper.

REFERENCES

Alt, J.C. & Teagle, D.A.H., 2000. Hydrothermal alteration and fluid fluxes in ophiolites and oceanic crust, *Spec. Pap.-Geol. Soc. Am.,* **349,** 273–282.

Argus, D.A., Gordon, R.G. & DeMets, C., 2011. Geologically current motion of 56 plates relative to the no-net-rotation reference frame, *Geochem. Geophys. Geosyst.,* **12,** 1-13.

Baran, J.M., Cochran, J.R., Carbotte, S.M. & Nedimovic, M.R., 2005. Variations in upper crustal structure due to variable mantle temperature along the Southeast Indian Ridge, *Geochem. Geophys. Geosyst.,* **6**(11), 1–21.

Baud, P. & Reuschlé, T., 1997. A theoretical approach to the propagation of interacting cracks, *Geophys. J. Int.,* **130,** 460–468.

Becker, K. *et al.*, 1989. Drilling deep into young rift oceanic crust, hole 504B, Costa Rica Rift, *Rev. Geophys.,* **27**(1), 79–102.

Blacic, T.M., Ito, G., Canales, J.P., Detrick, R.S. & Sinton, J., 2004. Constructing the crust along the Galapagos Spreading Center 91.3°–95.5° W: correlation of seismic layer 2A with axial magma lens and topographic characteristics, *J. geophys. Res.,* **109**(B10310), 1–19.

Bown, J.W. & White, R.S., 1994. Variation with spreading rate of oceanic crustal thickness and geochemistry, *Earth planet. Sci. Lett.,* **121**(3-4), 435–449.

Buck, W.R., Carbotte, S.M. & Mutter, C., 1997. Controls on extrusion at mid-ocean ridges, *Geology,* **25**(10), 935–938.

Canales, J.P., Dañobeitia, J.J., Detrick, R.S., Hooft, E.E.E., Bartolomé, R. & Naar, D.F., 1997. Variations in axial morphology along the Galápagos spreading center and the influence of the Galápagos hotspot, *J. geophys. Res.,* **102**(B12), 27341–27354.

Canales, J.P., Detrick, R.S., Toomey, D.R. & Wilcock, W.S.D., 2003. Segment-scale variations in the crustal structure of 150–300 kyr old fast

spreading oceanic crust (East Pacific Rise, 8°15′N–10°5′N) from wide-angle seismic refraction profiles, *Geophys. J. Int.,* **152**(3), 766–794.
Canales, J.P., Nedimovi, M.R., Kent, G.M., Carbotte, S.M. & Detrick, R.S., 2009. Seismic reflection images of a near-axis melt sill within the lower crust at the Juan de Fuca Ridge, *Nature,* **460**(7251), 89–93.
Canales, J.P., Tucholke, B.E. & Collins, J.A., 2004. Seismic reflection imaging of an oceanic detachment fault: Atlantis megamullion (Mid-Atlantic Ridge, 30°10′N), *Earth planet. Sci. Lett.,* **222,** 543–560.
Canales, J.P. *et al.*, 2005. Upper crustal structure and axial topography at intermediate spreading ridges: seismic constraints from the southern Juan de Fuca Ridge, *J. geophys. Res.,* **110**(B12104), 1–27.
Cannat, M., 1993. Emplacement of mantle rocks in the seafloor at mid-ocean ridges, *J. geophys. Res.,* **98**(B3), 4163–4172.
Cannat, M., Sauter, D., Mendel, V., Ruellan, E., Okino, K., Escartin, J., Combier, V. & Baala, M., 2006. Modes of seafloor generation at a melt-poor ultraslow-spreading ridge, *Geology,* **34**(7), 605–608.
Cann, J.R. *et al.*, 1997. Corrugated slip surfaces formed at ridge-transform intersections on the Mid-Atlantic Ridge, *Nature,* **385,** 329–332.
Carbotte, S.M., Marjanovic, M., Carton, H., Mutter, J.C., Canales, J.P., Nedimovi, M.R., Han, S. & Perfit, M.R., 2013. Fine-scale segmentation of the crustal magma reservoir beneath the East Pacific Rise, *Nat. Geosci.,* **6**(10), 866–870.
Carbotte, S.M. *et al.*, 2006. Rift topography linked to magmatism at the intermediate spreading Juan de Fuca Ridge, *Geology,* **34**(3), 209–212.
Carlson, R.L., 1998. Seismic velocities in the uppermost oceanic crust: age dependence and the fate of layer 2A, *J. geophys. Res.,* **103**(B4), 7069–7077.
Carlson, R.L. & Raskin, G.S., 1984. Density of the ocean crust, *Nature,* **311,** 555–558.
Chen, Y.J., 1992. Oceanic crustal thickness versus spreading rate, *Geophys. Res. Lett.,* **19**(8), 753–756.
Christensen, N.I., 1978. Ophiolites, seismic velocities and oceanic crustal structure, *Tectonophysics,* **47,** 131–157.
Christensen, N.I., 1979. Compressional wave velocities in rocks at high-temperatures and pressures, critical thermal-gradients, and crustal low-velocity zones, *J. geophys. Res.,* **84**(12), 6849–6857.
Christeson, G.L., Karson, J.A. & McIntosh, K.D., 2010. Mapping of seismic layer 2A/2B boundary above the sheeted dike unit at intermediate spreading crust exposed near the Blanco Transform, *Geochem. Geophys. Geosyst.,* **11**(3), doi:10.1029/2009GC002864.
Christeson, G.L., McIntosh, K.D. & Karson, J.A., 2007. Inconsistent correlation of seismic layer 2a and lava layer thickness in oceanic crust, *Nature,* **445**(7126), 418–421.
Christeson, G.L., Morgan, J.V & Warner, M.R., 2012. Shallow oceanic crust: full waveform tomographic images of the seismic layer 2A/2B boundary, *J. geophys. Res.,* **117,** 1–25.
Christeson, G.L., Purdy, G.M. & Fryer, G.J., 1992. Structure of young upper crust at the East Pacific Rise near 9°30′N, *Geophys. Res. Lett.,* **19**(10), 1045–1048.
Christeson, G.L., Shaw, P.R. & Garmany, J.D., 1997. Shear and compressional wave structure of the East Pacific Rise, 9°-10° N, *J. geophys. Res.,* **102,** 7821–7835.
Cochran, J.R., Sempere, J. & Team, S.S., 1997. The Southeast Indian Ridge between 88° E and 118° E: Gravity anomalies and crustal accretion at intermediate spreading rates, *J. geophys. Res.,* **102**(B7), 15 463–15 487.
Cohen, J.K. & Stockwell, J.W., 2010. CWP/SU: Seismic Un∗ x Release No. 42: an open source software package for seismic research and processing.
Collier, J.S. & Sinha, M.C., 1992. The Valu Fa Ridge: the pattern of volcanic activity at a back-arc spreading centre, *Mar. Geol.,* **104,** 243–263.
Dannowski, A., Grevemeyer, I., Ranero, C.R., Ceuleneer, G., Maia, M., Morgan, J.P. & Gente, P., 2010. Seismic structure of an oceanic core complex at the Mid-Atlantic Ridge, 22°19′N, *J. geophys. Res.,* **115**(B7), doi:10.1029/2009JB006943.
Davies, J.H. & Davies, D.R., 2010. Earth's surface heat flux, *Solid Earth,* **1,** 5–24.
Day, A.J., Peirce, C. & Sinha, M.C., 2001. Three-dimensional crustal structure and magma chamber geometry at the intermediate-spreading, back-arc Valu Fa Ridge, Lau Basin—results of a wide-angle seismic tomographic inversion, *Geophys. J. Int.,* **146,** 31–52.
Detrick, R.S., 1987. Multichannel seismic imaging of a crustal magma chamber along the EPR, *Nature,* **330,** 533–537.
Detrick, R.S., 1994. EW9416 cruise report, doi:10.7284/901288.
Detrick, R.S., Harding, A.J., Kent, G.M., Orcutt, J.A., Mutter, J.C. & Buhl, P., 1993. Seismic structure of the southern East Pacific Rise, *Science,* **259**(5094), 499–503.
Detrick, R.S. *et al.*, 2002. Correlated geophysical, geochemical, and volcanological manifestations of plume-ridge interaction along the Galápagos Spreading Center, *Geochem. Geophys. Geosyst.,* **3**(10), 1–14.
Dziak, R.P., Bohnenstiehl, D.R., Cowen, J.P., Baker, E.T., Rubin, K.H., Haxel, J.H. & Fowler, M.J., 2007. Rapid dike emplacement leads to eruptions and hydrothermal plume release during seafloor spreading events, *Geology,* **35**(7), 579–582.
Elderfield, H. & Schultz, A., 1996. Mid-ocean ridge hydrothermal fluxes and the chemical composition of the ocean, *Annu. Rev. Earth Planet. Sci,* **24,** 191–224.
Fontaine, F.J., Olive, J.A., Cannat, M., Escartin, J. & Perol, T., 2011. Hydrothermally-induced melt lens cooling and segmentation along the axis of fast-and intermediate-spreading centers, *Geophys. Res. Lett.,* **38**(14), 1–7.
Gregory, E.P.M., Hobbs, R.W., Peirce, C. & Wilson, D.J., 2017. Porosity, fracturing and alteration of young oceanic crust: new seismic analyses at borehole 504B, in Abstract T31C-1184 *presented at 2017 AGU Fall Meeting*, New Orleans, LA, 11–15 Dec.
Grevemeyer, I., Hayman, N.W., Peirce, C., Schwardt, M., Van Avendonk, H.J.A., Dannowski, A. & Papenberg, C., 2018b. Episodic magmatism and serpentinized mantle exhumation at an ultraslow-spreading centre, *Nat. Geosci.,* **11**(6), 444–448.
Grevemeyer, I., Ranero, C.R. & Ivandic, M., 2018a. Structure of oceanic crust and serpentinization at subduction trenches, *Geosphere,* **14**(2), 395–418.
Gutscher, M.A., Malavieille, J., Lallemand, S. & Collot, J.Y., 1999. Tectonic segmentation of the North Andean margin: impact of the Carnegie Ridge collision, *Earth planet. Sci. Lett.,* **168**(3-4), 255–270.
Han, S., Carbotte, S.M., Carton, H., Mutter, J.C., Aghaei, O., Nedimović, M.R. & Canales, J.P., 2014. Architecture of on- and off-axis magma bodies at EPR 9°37-40′N and implications for oceanic crustal accretion, *Earth planet. Sci. Lett.,* **390,** 31–44.
Harding, A.J., Kent, G.M. & Orcutt, J.A., 1993. A multichannel seismic investigation of upper crustal structure at 9° N on the East Pacific Rise: implications for crustal accretion, *J. geophys. Res.,* **98**(B8), 13925–13944.
Haughton, G., Hobbs, R.W. Murton B.J. & Henstock, T., 2018. Spreading ridge lower order segmentations effect on large scale fault heave, in Abstract EGU2018-15830, *presented at 2018 EGU General Assembly*, Vienna, 8–13 Apr.
Herron, T.J., 1982. Lava flow layer - East Pacific Rise, *Geophys. Res. Lett.,* **9**(1), 17–20.
Hey, R., 1977. A new class of "pseudofaults" and their bearing on plate tectonics: a propagating rift model, *Earth planet. Sci. Lett.,* **37**(2), 321–325.
Hobbs, R.W. & Peirce, C., 2015. RRS James Cook JC114 cruise report. https://www.bodc.ac.uk/resources/inventories/cruise_inventory/reports/jc114.pdf.
Hooft, E.E.E. & Detrick, R.S., 1995. Relationship between axial morphology, crustal thickness, and mantle temperature along the Juan de Fuca and Gorda Ridges, *J. geophys. Res.,* **100**(B11), 22 499–22 508.
Hooft, E.E.E., Detrick, R.S. & Kent, G.M., 1997. Seismic structure and indicators of magma budget along the Southern East Pacific Rise, *J. geophys. Res.,* **102**(B12), 27 319–27 340.
Houtz, R. & Ewing, J., 1976. Upper crustal structure as a function of plate age, *J. geophys. Res.,* **81**(14), 2490–2498.
Kelemen, P.B., Koga, K. & Shimizu, N., 1997. Geochemistry of gabbro sills in the crust-mantle transition zone of the Oman ophiolite implications

for the origin of the oceanic lower crust, *Earth planet. Sci. Lett.,* **146,** 475–488.

Kent, G., Harding, A. & Orcutt, J., 1990. Evidence for a smaller magma chamber beneath the East Pacific Rise at 9°30′N, *Nature,* **344,** 650–653.

Kent, G.M., Harding, A.J. & Orcutt, J.A., 1993. Distribution of magma beneath the East Pacific Rise between the Clipperton Transform and the 9°17′N deval from forward modeling of common depth point data, *J. geophys. Res.,* **98**(93), 13 945–13 969.

Kent, G.M. *et al.*, 2000. Evidence from three-dimensional seismic reflectivity images for enhanced melt supply beneath mid-ocean ridge discontinuities, *Nature,* **406,** 614–618.

Krijgsman, W., Hilgen, F.J., Raffi, I., Sierro, F.J. & Wilson, D.S., 1999. Chronology, causes and progression of the Messinian salinity crisis, *Nature,* **400**(6745), 652–655.

Lin, J. & Phipps Morgan, J., 1992. The spreading rate dependence of three-dimensional mid-ocean ridge gravity structure, *Geophys. Res. Lett.,* **19**(1), 13–16.

Liu, Z. & Buck, W.R., 2018. Magmatic controls on axial relief and faulting at mid-ocean ridges, *Earth planet. Sci. Lett.,* **491,** 226–237.

Lomax, A., Virieux, J., Volant, P. & Berge-Thierry, C., 2000. Probabilistic earthquake location in 3D and layered models: introduction of a Metropolis-Gibbs method and comparison with linear locations, in *Advances in Seismic Event Location,* pp. 101–134, eds Thurber, C.H. & Rabinowitz, N., Kluwer, doi:10.1007/978-94-015-9536-0_5.

Lonsdale, P., 1983. Overlapping rift zones at the 5.5° S offset of the East Pacific Rise, *J. geophys. Res.,* **88,** 9393–9406.

Lonsdale, P. & Klitgord, K.D., 1978. Structure and tectonic history of the eastern Panama Basin, *Bull. Geol. Soc. Am.,* **89**(7), 981–999.

Lowell, R. P., Farough, A., Hoover, J. & Cummings, K., 2013. Characteristics of magma-driven hydrothermal systems at oceanic spreading centers, *Geochem. Geophys. Geosyst.,* **14**(6), 1756–1770.

Lowell, R.P., Van Cappellen, P. & Germanovich, L.N., 1993. Silica precipitation in fractures and the evolution of permeability in hydrothermal upflow zones, *Science,* **260,** 192–194.

Lowell, R.P. *et al.*, 2020. Magma-hydrothermal interactions at the Costa Rica Rift from data collected in 1994 and 2015, *Earth planet. Sci. Lett.,* **531,** doi:10.1016/j.epsl.2019.115991.

Macdonald, K.C. & Fox, P.J., 1983. Overlapping spreading centres: new accretion geometry on the East Pacific Rise, *Nature,* **302**(5903), 55–58.

Macdonald, K.C., Scheirer, D.S. & Carbotte, S.M., 1991. Mid-ocean ridges: discontinuities, segments and giant cracks, *Science,* **253,** 986–994.

Macdonald, K.C., Sempere, J.C., Fox, P.J. & Tyce, R., 1987. Tectonic evolution of ridge-axis discontinuities by the meeting, linking, or self-decapitation of neighboring ridge segments, *Geology,* **15**(11), 993–997.

Macdonald, K.C. *et al.*, 1988. A new view of the mid-ocean ridge from the behaviour of ridge-axis discontinuities, *Nature,* **335**(6187), 217.

Macdonald, KC., Sempéré, J.-C. & Fox, P.J., 1984. East Pacific Rise from Siqueiros to Oroco Fracture Zones: along-strike continuity of axial neovolcanic zone and structure and evolution of overlapping spreading centers, *J. geophys. Res.,* **89**(B7), 6049–6069.

MacGregor, L.M., Constable, S. & Sinha, M.C., 1998. The RAMESSES experiment-III. Controlled source electromagnetic sounding of the Reykjanes Ridge at 57°45′N, *Geophys. J. Int.,* **135,** 773–789.

Maclennan, J., 2005. Cooling of the lower oceanic crust, *Geology,* **33**(5), 357–360.

Ma, L.Y. & Cochran, R., 1997. Bathymetric roughness of the Southeast Indian Ridge: implications for crustal accretion at intermediate spreading rate mid-ocean ridges, *J. geophys. Res.,* **102**(97), 17 697–17 711.

Marjanović, M., Carbotte, S.M., Carton, H.D., Nedimović, M.R., Canales, J.P. & Mutter, J.C., 2018. Crustal magmatic system beneath the East Pacific Rise - segmentation and crustal melt transport at fast-spreading ridges, *Geochem. Geophys. Geosyst.,* **19,** 4584–4611.

Mendel, V., Sauter, D., Rommevaux-Jestin, C., Patriat, P., Lefebvre, F. & Parson, L.M., 2003. Magmato-tectonic cyclicity at the ultra-slow spreading Southwest Indian Ridge: evidence from variations of axial volcanic ridge morphology and abyssal hills pattern, *Geochem. Geophys. Geosyst.,* **4**(5), doi:10.1029/2002GC000417.

Meschede, M. & Barckhausen, U., 2001. The relationship of the Cocos and Carnegie ridges: age constraints from paleogeographic reconstructions, *Int. J. Earth Sci.,* **90**(2), 386–392.

Minshull, T.A., Sinha, M.C. & Peirce, C., 2005. Multi-disciplinary, subseabed geophysical imaging – a new pool of 28 seafloor instruments in use by the United Kingdom Ocean Bottom Instrument Consortium, *Sea Technology,* **46**(10), 27–31.

Morales Maqueda, M.A., 2015. RRS James Cook JC112/3 cruise report. https://www.bodc.ac.uk/resources/inventories/cruise_inventory/report/15034/.

Morell, K.D., 2015. Late Miocene to recent plate tectonic history of the southern Central America convergent margin, *Geochem. Geophys. Geosyst.,* **16,** 3362–3382.

Navin, D.A., Peirce, C. & Sinha, M.C., 1998. The RAMESSES experiment — II. Evidence for accumulated melt beneath a slow spreading ridge from wide-angle refraction and multichannel reflection seismic profiles, *Geophys. J. Int.,* **135**(3), 746–772.

Newman, K.R., Nedimovi, M.R., Canales, J.P. & Carbotte, S.M., 2011. Evolution of seismic layer 2B across the Juan de Fuca Ridge from hydrophone streamer 2-D traveltime tomography, *Geochem. Geophys. Geosyst.,* **12**(5), doi:10.1029/2010GC003462.

Peirce, C., Gardiner, A. & Sinha, M., 2005. Temporal and spatial cyclicity of accretion at slow-spreading ridges — evidence from the Reykjanes Ridge, *Geophys. J. Int.,* **163,** 56–78.

Peirce, C., Reveley, G., Robinson, A.H., Funnell, M.J., Searle, R.C., Simão, N.M., MacLeod, C.J. & Reston, T.J., 2019. Constraints on crustal structure of adjacent OCCs and segment boundaries at 13° N on the Mid-Atlantic Ridge, *Geophys. J. Int.,* **217,** 988–1010.

Peirce, C. & Sinha, M.C., 2008. Life and death of axial volcanic ridges: segmentation and crustal accretion at the Reykjanes Ridge, *Earth planet. Sci. Lett.,* **274,** 112–120.

Phipps Morgan, J. & Chen, Y.J., 1993. Magma injection, hydrothermal circulation, and crustal flow, *J. Geol.,* **98**(B4), 6283–6297.

Ranero, C. & Reston, T.J., 1999. Detachment faulting at oceanic core complexes, *Geology,* **27,** 983–986.

Reston, T., 2018. Flipping detachments: the kinematics of ultraslow spreading ridges, *Earth planet. Sci. Lett.,* **503,** 144–157.

Reston, T.J. & Ranero, C.R., 2011. The 3-D geometry of detachment faulting at mid-ocean ridges, *Geochem. Geophys. Geosyst.,* **12**(7), 1–19.

Sandwell, D.T., Müller, R.D., Smith, W.H.F., Garcia, E. & Francis, R., 2014. New global marine gravity model from CryoSat-2 and Jason-1 reveals buried tectonic structure, *Science,* **346**(6205), 65–67.

Scheirer, D.S. & Macdonald, K.C., 1993. Variation in cross-sectional area of the Axial Ridge along the East Pacific Rise: evidence for the magmatic budget of a fast spreading center, *J. Geol.,* **98**(B5), 7871–7885.

Sempéré, J. & Macdonald, K.C., 1986. Overlapping spreading centres: implications from crack growth simulation by the displacement discontinuity method, *Tectonics,* **5**(1), 151–163.

Singh, S.C., Kent, G.M., Collier, J.S., Harding, A.J. & Orcutt, J.A., 1998. Melt to mush variations in crustal magma properties along the ridge crest at the southern East Pacific Rise, *Nature,* **394,** 219–222.

Sinha, M.C., Constable, S.C., Peirce, C., White, A., Heinson, G., MacGregor, L.M. & Navin, D.A., 1998. Magmatic processes at slow spreading ridges: implications of the RAMESSES experiment at 57°45′N on the Mid-Atlantic Ridge, *Geophys. J. Int.,* **135,** 731–745.

Sinha, M.C., Navin, D.A., MacGregor, L.M., Constable, S., Peirce, C., White, A., Heinson, G. & Inglis, M., 1997. Evidence for accumulated melt beneath the slow-spreading Mid-Atlantic Ridge, *Phil.. Trans. R. Soc. A,* **355,** 233–253.

Sinton, J., Detrick, R., Canales, J.P. & Behn, M., 2003. Morphology and segmentation of the western Galapagos Spreading Center, 90.5°-98° W: plume-ridge interaction at an intermediate spreading ridge, *Geochem. Geophys. Geosyst.,* **4**(12), 1–26.

Sinton, J.M. & Detrick, R.S., 1992. Mid-ocean ridge magma chambers, *J. geophys. Res.,* **97**(B1), 197–216.

Small, C. & Abbott, D., 1998. Subduction obstruction and the crack-up of the Pacific plate, *Geology,* **26**(9), 795–798.

Spencer, S., Smith, D.K., Cann, J.R., Lin, J. & Allister, E.M., 1997. Structure and stability of non-transform discontinuities on the Mid-Atlantic Ridge between 24° N and 30° N, *Mar. Geophys. Res.,* **19,** 339–362.

Stein, C.A. & Stein, S., 1994. Constraints on hydrothermal heat flux through the oceanic lithosphere from global heat flow, *J. geophys. Res.,* **99**(B2), 3081–3095.

Talwani, M., Worzel, J.L. & Landisman, M., 1959. Rapid gravity computations for two-dimensional bodies with application to the Mendocino submarine fracture zone, *J. geophys. Res.,* **64**(1), 49–59.

Tolstoy, M., Waldhauser, F., Bohnenstiehl, D.R., Weekly, R.T. & Kim, W., 2008. Seismic identification of along-axis hydrothermal flow on the East Pacific Rise, *Nature,* **451,** 181–185.

Tong, C.H. *et al.*, 2002. Asymmetric melt sills and upper crustal construction beneath overlapping ridge segments: implications for the development of melt sills and ridge crests, *Geology,* **30**(1), 83–86.

Tong, C.H. *et al.*, 2003. Influence of enhanced melt supply on upper crustal structure at a mid-ocean ridge discontinuity: a three-dimensional seismic tomographic study of 9° N East Pacific Rise, *J. geophys. Res.,* **108**(B10), 1–14.

Turner, I.M., Peirce, C. & Sinha, M.C., 1999. Seismic imaging of the axial region of the Valu Fa Ridge, Lau Basin - the accretionary processes of an intermediate back-arc spreading ridge, *Geophys. J. Int.,* **138**(2), 495–519.

Tyler, S., Bull, J.M., Parson, L.M. & Tuckwell, G.W., 2007. Numerical modelling of non-transform discontinuity geometry: implications for ridge structure, volcano-tectonic fabric development and hydrothermal activity at segment ends, *Earth planet. Sci. Lett.,* **257**(1-2), 146–159.

van Ark, E.M. *et al.*, 2007. Seismic structure of the Endeavour Segment, Juan de Fuca Ridge: correlations with seismicity and hydrothermal activity, *J. geophys. Res.,* **112,** 1–22.

Vargas, C.A., Pulido, J.E. & Hobbs, R.W., 2018. Thermal structure of the Panama Basin by analysis of seismic attenuation, *Tectonophysics,* **730,** 81–99.

Vera, E.E., Mutter, J.C., Buhl, P., Orcutt, J.A., Harding, A.J., Kappus, M.E., Detrick, R.S. & Brocher, T.M., 1990. The structure of 0- to 0.2-m.y.-old oceanic crust at 9° N on the East Pacific Rise from expanded spread profiles, *J. geophys. Res.,* **95**(B10), 15 529–15 556.

Wanless, V.D. & Shaw, A.M., 2012. Lower crustal crystallization and melt evolution at mid-ocean ridges, *Nat. Geosci.,* **5**(9), 651–655.

Weekly, R.T., Wilcock, W.S.D., Toomey, D.R., Hooft, E.E.E. & Kim, E., 2014. Upper crustal seismic structure of the Endeavour segment, Juan de Fuca Ridge from traveltime tomography: implications for oceanic crustal accretion, *Geochem. Geophys. Geosyst.,* **15**(4), 1296–1315.

Wessel, P., 2010. Tools for analyzing intersecting tracks: the x2sys package, *Comput. Geosci.,* **36**(3), 348–354.

Wessel, P. & Smith, W.H.F., 1998. New, improved version of generic mapping tools released, *EOS, Trans. Am. Geophys. Un.,* **79**(47), 579–579.

White, R.S., McKenzie, D. & O'Nions, K., 1992. Oceanic crustal thickness from seismic measurements and rare earth element inversions, *J. geophys. Res.,* **97**(B13), 19 683–19 715.

White, S.M., Meyer, J.D., Haymon, R.M., Macdonald, K.C., Baker, E.T. & Resing, J.A., 2008. High-resolution surveys along the hot spot–affected Galápagos Spreading Center: 2. influence of magma supply on volcanic morphology, *Geochem. Geophys. Geosyst.,* **9**(9), 1–29.

Wilcock, W.S.D., Archer, S.D. & Purdy, G.M., 2002. Microearthquakes on the Endeavour segment of the Juan de Fuca Ridge, *J. geophys. Res.,* **107**(B12), 1–21.

Wilson, D.J., Robinson, A.H., Hobbs, R.W., Peirce, C. & Funnell, M.J., 2019. Does intermediate spreading-rate oceanic crust result from episodic transition between magmatic and magma-dominated, faulting-enhanced spreading? – the Costa Rica Rift example, *Geophys. J. Int.,* **228**(3), 1617–1641.

Wilson, D.S., 1990. Kinematics of overlapping rift propagation with cyclic rift failure, *Earth planet. Sci. Lett.,* **96,** 384–392.

Wilson, D.S. & Hey, R.N., 1995. History of rift propagation and magnetization intensity for the Cocos-Nazca spreading Center, *J. geophys. Res.,* **100**(95), 10041.

Zelt, C.A., 1998. Lateral velocity resolution from three-dimensional seismic refraction data, *Geophys. J. Int.,* **135**(3), 1101–1112.

Zelt, C.A., 1999. Modelling strategies and model assessment for wide-angle seismic traveltime data, *Geophys. J. Int.,* **139,** 183–204.

Zelt, C.A. & Barton, P.J., 1998. Three-dimensional seismic refraction tomography: a comparison of two methods applied to data from the Faeroe Basin, *J. geophys. Res.,* **103**(B4), 7187–7210.